Supplementary Information

Copper with an atomic-scale spacing for efficient electrocatalytic co-reduction of carbon dioxide and nitrate to urea

Seokmin Shin[a], Siraj Sultan[a], Zong-Xian Chen[b], Hojeong Lee[a], Hansaem Choi[a], Tae-Ung Wi[c], Changhyun Park[a], Taewon Kim[a], Chanhee Lee[a], Jihong Jeong[a], Hyeju Shin[d], Tae-Hee Kim[d], HyungKuk Ju[e], Hyung Chul Yoon[e], Hyun-Kon Song*[a], Hyun-Wook Lee*[a], Mu-Jeng Cheng*[b], Youngkook Kwon*[a,f]

[a]School of Energy and Chemical Engineering, UNIST, Ulsan 44919, Korea.
[b]Department of Chemistry, National Cheng Kung University, Tainan 701, Taiwan.
[c]Department of Chemical and Biomolecular Engineering, Rice University, Houston, Texas, 77005, United States.
[d]Ulsan Advanced Energy Technology R&D Center, Korea Institute of Energy Research (KIER), Ulsan 44776, Korea.
[e]Climate Change Research Division, Korea Institute of Energy Research (KIER), Daejeon 34129, Korea
[f]Graduate School of Carbon Nuetrality, UNIST, Ulsan 44919, Korea

*Correspondence and requests for materials should be addressed to Y.K. (ykwon@unist.ac.kr).

Methods

Synthesis of d_s in Cu_2O

A bare Cu_2O nanoparticle (< 50 nm; Sigma-Aldrich) was lithiated and then delithiated to develop inter-particular spacings within the nanoparticles. 2032-coin cells and the monolayer pouch-type cells were assembled for lithiating and delithiating Cu_2O. A polyethylene separator (NH716, Asahi) was placed between a Cu_2O-loaded electrode and a Li metal foil. A Cu_2O-containing slurry loaded on a copper foil by 7.0 mg cm^{-2} was dried for 24 h in a vacuum at 110 °C. The slurry was prepared by mixing Cu_2O and PVdF (solef5130, Solvay) at 9:1 wt% in N-methyl-2-pyrrolidinone (NMP; Daejung). 1 M $LiPF_6$ in a mixture of ethylene carbonate (EC) and ethyl methyl carbonate (EMC) at a volume ratio of 3:7 was used as the electrolyte (40µl for coin-type cell and 300µl for pouch-type cell). An electrode was cut-off in 16 pi or 3 x 4.5 cm^2. Ar-filled glove box (Mbraun; <0.1 ppm O_2 and H_2O) was used for coin- cells assembling and electrolytes preparation. Temperature-controlled dry room was used for pouch-type cells assembly. A Cu_2O electrode was lithiated at 0.1C (C-rate, equivalent to 0.38 mA cm^{-2} up to 0.85 V, 0.7 Vand 0 V (0.01 V) with respect to the lithium metal counter electrode. For the delithiation step, same C-rate up to 3.0 V_{Li} was applied. The samples were washed sequentially with NMP, ethanol, acetone, and 0.05 M of acetic acid to remove residual lithium sources such as Li_2O. Samples were rinsed with DI water between each washing process. The washing process was repeated a total of 3 times to finally prepare the catalyst.

Nanochannel identification

The atomic-scale spacings (d_s) in the lithiated and delithiated Cu_2O samples were measured through an *in-situ* and *ex-situ* transmission electron microscope (TEM) analysis. The real-time data was acquired by using a TEM (Tecnai G2 F20 X-TWIN, FEI) with an acceleration voltage of 200 kV and an *in-situ* holder (Dual-Probe STM-TEM *in-situ* holder, Nanofactory Instruments) with two electrodes. One was a Cu tip with Cu_2O nanoparticles as a working electrode and the other was a tungsten tip with lithium metal as a counter and reference electrode. On the lithium metal surface, Li_2O occurs due to air exposure for several seconds, which acts as a solid electrolyte. Lithiation was performed by applying a 0.5 V bias between the two electrodes.

Ex-situ TEM analysis was performed using a high-resolution transmission electron microscope (JEM-2100F, HRTEM, and JEOL). Bright and dark field images for measuring the gap at each state were performed by a scanning TEM (JEM-2100F, STEM, and JEOL) at the acceleration voltage of 200 kV.

Material identification

X-ray diffraction patterns (XRD), X-ray photoelectron spectra (XPS), and X-ray adsorption spectra (XAS) were obtained to identify the material composition of nanochannel Cu_2O experiencing lithiation and then de-lithiation. XRD: Rigaku D/MAX2500V/PC at 40 kV and 200 mA copper rotating anode. XPS: XPS system by Thermo Fisher with Al Kα (hν = 1486.6 eV). XAS: The beamline 6D in Pohang Accelerator Laboratory (PAL) at 3.5 GeV with 400 mA by transmittance signals for *ex-situ* analysis and fluorescence signals for *in-situ* analysis.

Electrochemical measurements

The electrochemical experiments including cyclic voltammograms (CV), linear sweep voltammograms (LSV), and chronopotentiometry were conducted with a potentiostat (VMP3 and VSP-300, BioLogic). For the electrochemical performance evaluation of our synthesized catalysts, we deposed the ink of the catalyst with a loading density of 0.5 mg cm^{-2} on the gas diffusion electrode (GDE, Sigracet, Fuel cell store) and used it as a cathode part in a gas-tight flow-type cell. CO_2 gas as reactant was introduced to the gas chamber of the cell at the rate of 20 mL min^{-1} while the electrolyte was circulated at a speed of 8 mL min^{-1}. A dimensionally stable anode (DSA, HS materials) was used as an anode while Hg/HgO (1 M KOH) was used as a reference electrode. To avoid the re-oxidation of products at the anode, the working and reference electrodes were separated from the anodic chamber through an anion exchange membrane (Sustanion, Dioxide Materials). All the potentials reported in this work were converted into reversible hydrogen electrode (E vs. RHE) with the equation of $E_{RHE} = E_{Hg/HgO} + E^0_{Hg/HgO} + 0.059*pH$. LSVs and CPs are also IR-corrected.

Product analysis

The gaseous products such as ethylene, carbon monoxide, methane and hydrogen were analyzed quantitatively and qualitatively through online gas chromatography (GC, iGC 7200A, DS Science). The outlet of the gaseous chamber in the electrochemical cell was directly connected to the GC and repeatedly injected into GC during the operation (time interval of 20 min during 1.5 h chronoamperometry or chronopotentiometry experiments).

The C-N coupled liquid products (Urea, acetamide and formamide) was analyzed using ^{1}H-NMR analysis with 400 MHz Fourier transform nuclear magnetic resonance (400 MHz FT-NMR, AVANCE III HD, Bruker). The carbon-containing liquid products (Formate, methanol, acetate, and ethanol) were analyzed through high-performance liquid chromatography (HPLC, 1260 Infinity II, Agilent Technologies). Nucleogel Sugar 810 column and a refractive index detector equipped with 5 mM sulfuric acid were used as an eluent. The possible liquid by-products such as ammonia and hydroxylamine during the CR-CO_2/NO_3^- or in sole NO_3^-RR were analyzed by ion chromatography (Thermo Scientific Dionex Aquion and AS-DV Autosampler) equipped with Dionex™ IonPac™ CS12A column. 4 mM HNO_3 solution was used as an eluent. For all the liquid products, Faradaic efficiency (%) was calculated by

measuring the charge required to produce the analyzed product concentration divided by the total charge passed during the electrolysis.

Calculation of FE and urea yield rate
The urea yield rate and FE of products are calculated by the following equations:

$$Urea\ yield\ rate\ \left(g\ h^{-1}\ mg_{cat}^{-1}\right) = \frac{C_{urea}(g\ mL^{-1}) \times V(mL)}{t\ (h)\ \times\ m_{cat}(mg)}$$

(1)

$$FE\ (\%) = \frac{n_e\ \times\ n_{product}(mol) \times F(C\ mol^{-1})}{Q\ (C)} \times 100\ (\%)$$

(2)

Where C_{urea} and V are the measured urea concentration and electrolyte volume. m_{cat} is the amount of catalyst loading which is 0.5 mg cm^{-2} in this work. F is the Faraday constant (96,485 C mol^{-1}) and Q is the total charge during the reaction. n_e is the number of electron transfers for each reaction and $n_{product}$ is the mol of each product.

In-situ Raman spectroscopy measurements
In-situ Raman spectroscopy measurements were performed using XperRAM S confocal microscope (objective lens with 50 times magnification, 532 nm laser) in a custom-made flow-type Raman cell with 1 M KOH electrolyte. As-prepared catalysts treated by the surface-enhanced Raman spectroscopy (SERS) method were deposited on GDE and used as working electrodes, while a Ni-Fe-Mo and an Ag/AgCl (saturated with KCl) were used as counter and reference electrodes, respectively. *In-situ* Raman spectroscopy measurements during CO_2 & NO_3^- co-reduction reaction (CR-CO_2/NO_3^-) were performed with 1 M KOH added with 0.1 M KHCO$_3$ electrolyte and CO_2 gas was continuously supplied to the gas chamber during the reaction.

CO_2-Temperature programmed desorption (CO_2-TPD) measurements
To perform CO_2-TPD, 50 mg of catalyst was calcined in Helium (He) at 200 °C for 1 hour in a quartz tube. The sample was then cooled to 50 °C to adsorb CO_2 for 30 min. The system was purged with He for 30 min to remove weakly adsorbed species. The TCD signal was stabilized for 1 hour, and the TPD program started by heating the sample to 600 °C at a rate of 10 °C/min.

Computational details
PBE-D3 combined with projector augmented wave pseudopotentials (400 eV energy cutoff) as implemented in the Vienna ab initio Simulation Package (VASP) was used for all DFT calculations. We used the Gaussian-smearing method (k_BT = 0.1 eV for slabs and 0.01 eV for CO_2) to accelerate SCF convergence, and the electronic energies at T = 0 K were obtained through extrapolation. For slab calculations, a Monkhorst-Pack k-point net of 3×3×1 was used to sample the reciprocal space, whereas only the gamma point was considered for gaseous CO_2. Spin-polarized DFT was used for all calculations.

The bare copper surface was modeled using Cu(111) with three 3×3 layers cleaved from bulk face-centered cubic copper with a cell parameter of 3.615 Å. During geometric optimizations, the top two layers and surface-bound species were allowed to relax, and the bottom layer was fixed in its bulk position. Copper with an atomic gap was modelled using two Cu(111) surfaces each composed of three 3×3 layers. During geometric optimizations, the bottom layer of the lower surface and the top layer of the up surface were fixed in their bulk position, whereas the rest of the model including the adsorbates was allowed to relax. A vacuum of at least 30 Å was introduced to the slab models to avoid interactions between two adjacent cells along the *z*-direction. To compute the energy of CO_2, a cubic simulation box with a volume of 20*20*20 Å^3 was employed.

The transition states were located using the dimer method and further verified by vibrational frequency calculations where only one imaginary frequency was present. For each coupling of *CO/*COOH with the N_1 species, two transition states were located. One has both C_1 and N_1 adsorbates on the lower surface, whereas the other has one adsorbate on the lower surface and the other on the upper surface. Our calculations showed that the former one is more facile.

The free energies of the slab systems were calculated based on the following equation:

$$G = E_{elec} + ZPVE + \sum_v \frac{h\nu}{e^{h\nu/k_BT} - 1} - T \times S_{vib}$$

(3)

The vibrational frequencies (hv) were only evaluated for adsorbates by evaluating the partial Hessian matrix via the finite difference approach to obtain the zero-point vibrational energy (ZPVE) and vibrational entropy (S_{vib}). The free energies of CO_2 were calculated using the following equation:

$$G = E_{elec} + ZPVE + \sum_{v} \frac{hv}{e^{hv/k_B T} - 1} + \frac{n}{2} k_B T - T \times (S_{trans} + S_{rot} + S_{vib})$$

(4)

where n is seven. E_{elect} was obtained using VASP, and the ZPVE, a vibrational component of the internal energy, S_{vib}, S_{rot}, and S_{trans} were obtained using Gaussian09 at the PBE-D3/6-311++G** level of theory.

Supplementary Notes

Lithiation and De-lithiation process during synthesis of d_s in Cu_2O

Oxide-based materials, including Cu_2O, are categorized as conversion materials in the field of lithium-ion battery applications and generally undergo the following reaction: ($MO + 2Li + 2e^- \rightarrow M + Li_2O$) - (1)

Moreover, Li_2O has low chemical activity and is known to decompose easily. In conventional lithium-ion battery systems, conversion materials typically experience a change in particle size to form nanoparticles upon lithiation. For Cu_2O, this conversion, or lithiation, occurs through the following reaction: ($Cu_2O + 2Li^+ + 2e^- \rightarrow 2Cu + Li_2O$) - (2)

The changes in morphology and lattice during the corresponding lithiation process were presented with detailed explanations in the main text (Fig. 2 and Fig. S4, 7, etc.). However, in the de-lithiation process (step IV in our manuscript), the above reaction (2) is simply reversed ($Cu_2O + 2Li^+ + 2e^- \leftarrow 2Cu + Li_2O$), during this de-lithiation step, the metallic Cu is oxidized back to Cu_2O. From HR-TEM and STEM analysis we note that the de-lithiation step do not change the particle size (the particle size is almost similar to that of lithiated Cu catalysts) but only increase the d_s between the copper facets (Fig. S7). Therefore, the catalyst that underwent the de-lithiation process is mainly composed of Cu_2O, with some unoxidized Cu and Li_2O. After the de-lithiation process, we removed Li_2O through a washing process, analysed the catalyst, and referred to it as 15Å-Cu.

When considering the formation of d_s, lithiation and de-lithiation tend to increase in accordance with the degree of lithiation (3 Å, 6 Å, and 12 Å) and through de-lithiation (15 Å). Therefore, in this study, lithiation and de-lithiation are considered as an integrated process in the goal of creating d_s. Although the degree of mixing of oxide and metallic state may differ depending on the lithiation/de-lithiation process, the corresponding electronic state does not impact the morphology and formation of d_s. Furthermore, all catalysts are reduced to metallic Cu during $CR-CO_2/NO_3^-$. Moreover, adopting this perspective, the experimental analysis of catalysts 6Å-Cu and 15Å-Cu, which respectively underwent lithiation and de-lithiation, revealed that the components of each catalyst were not significantly different. However, a significant disparity was observed in the electrochemical performance, leading us to conduct analysis of chemical adsorption of CO_2 behavior. Hence, we conducted CO_2 temperature programmed desorption (CO_2-TPD) experiments and present the results in Fig. S31 (ESI). The CO_2 desorption peak intensity showed a tendency in the order of 6Å-Cu > 15Å-Cu > Cu, and the peak location was in the order of 6Å-Cu (281.6 °C) > 15Å-Cu (276.3 °C) > Cu (268.2 °C). This indicated that 6Å-Cu had a stronger degree of chemisorption and more CO_2 adsorption capacity.
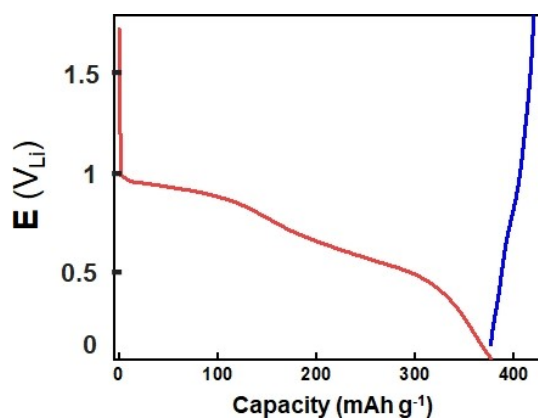
Fig. S1. Voltage profile of lithiation and delithiation of Cu₂O. Voltage profile was plotted with corresponding capacity during lithiation and delithiation. A voltage profile provided in Fig. 1a is normalized based on this voltage profile by dividing specific capacity of each lithiation and de lithiation step to present x-axis as a ratio.
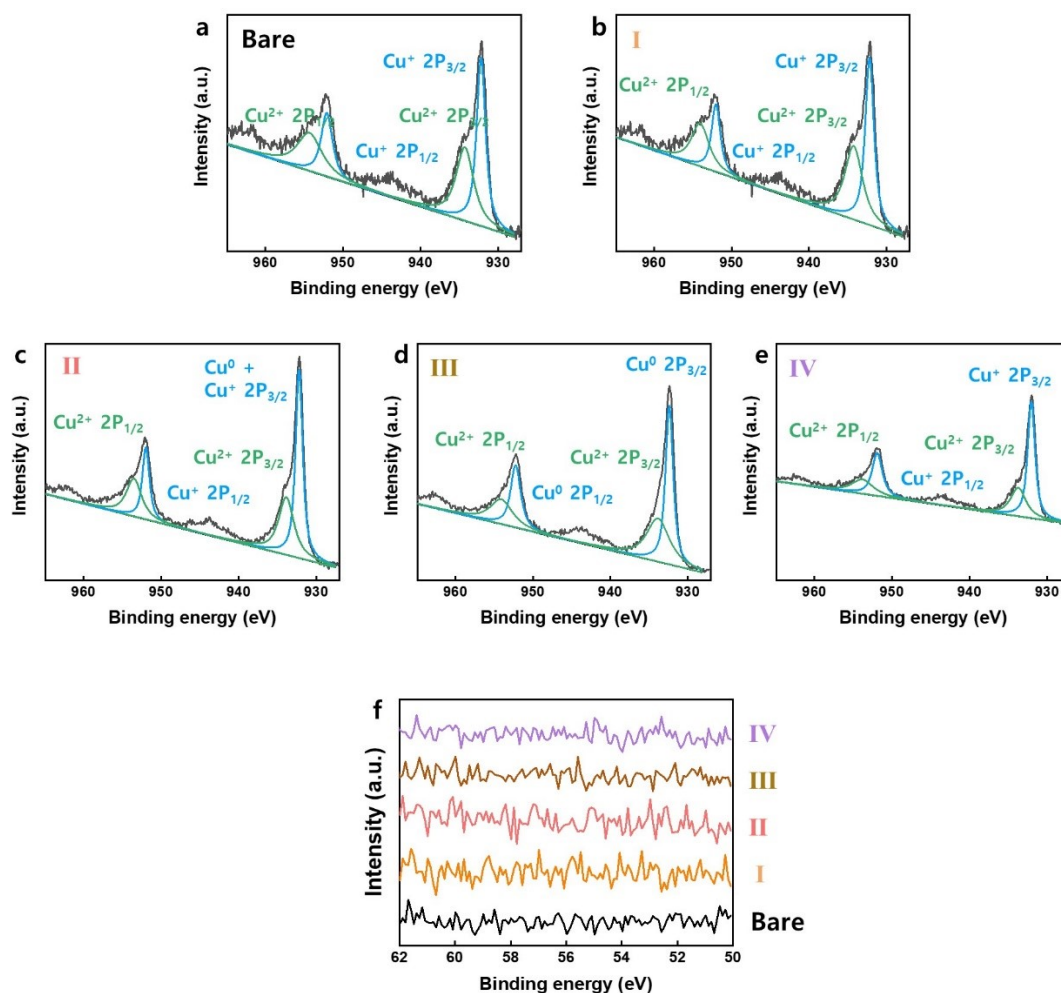

Fig. S2. X-ray-photoelectron-spectroscopic (XPS) spectra analysis of bare Cu₂O and its sisters with atomic scale spacings. (**a-e**) Copper elements of Cu₂O catalysts in Cu 2p XPS spectra. (**f**) Lithium elements of Cu₂O catalysts in Li 1s XPS spectra.
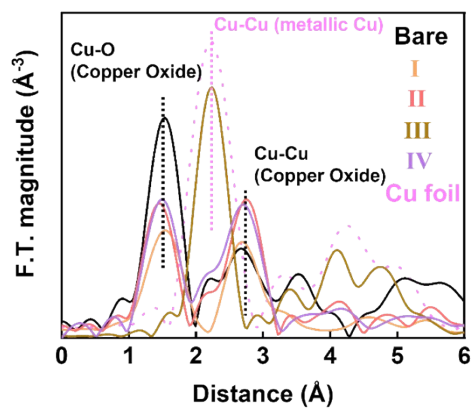
Fig. S3. Radial distances between Cu and its surrounding elements. *Ex-situ* extended X-ray absorption fine structure spectra analysis was conducted.
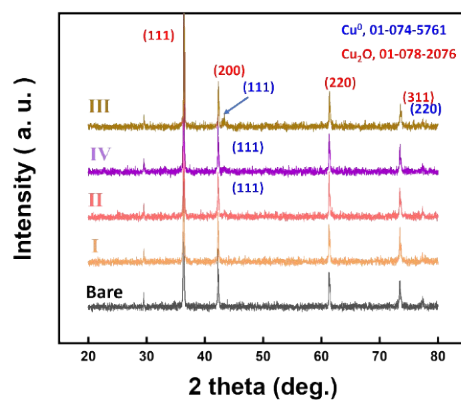

Fig. S4. Crystallographic identification of bare Cu_2O and samples with lithiation in powder X-ray diffraction (PXRD) patterns.
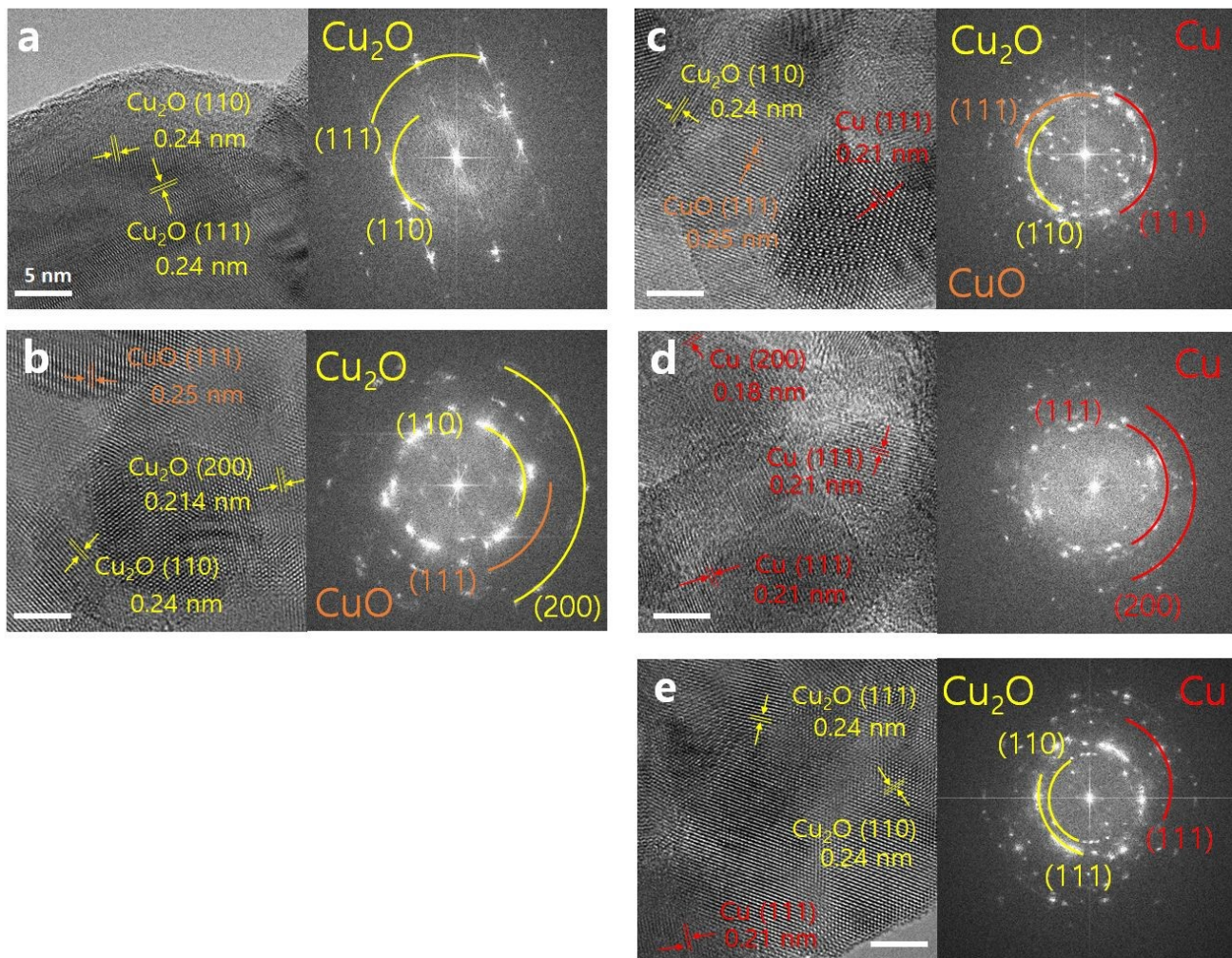
Fig. S5. HR-TEM images with FFT analysis. Lattices and facets were analysed on TEM images with an inset of FFT. (a) Bare Cu_2O, (b) Step I, (c) Step II, (d) Step III, and (e) step IV. We note that all the samples are chemically de-lithiated and CuO lattices are observed in the HR-TEM image of (a-c) originating from the easily oxidative characteristic of Cu_2O to CuO.
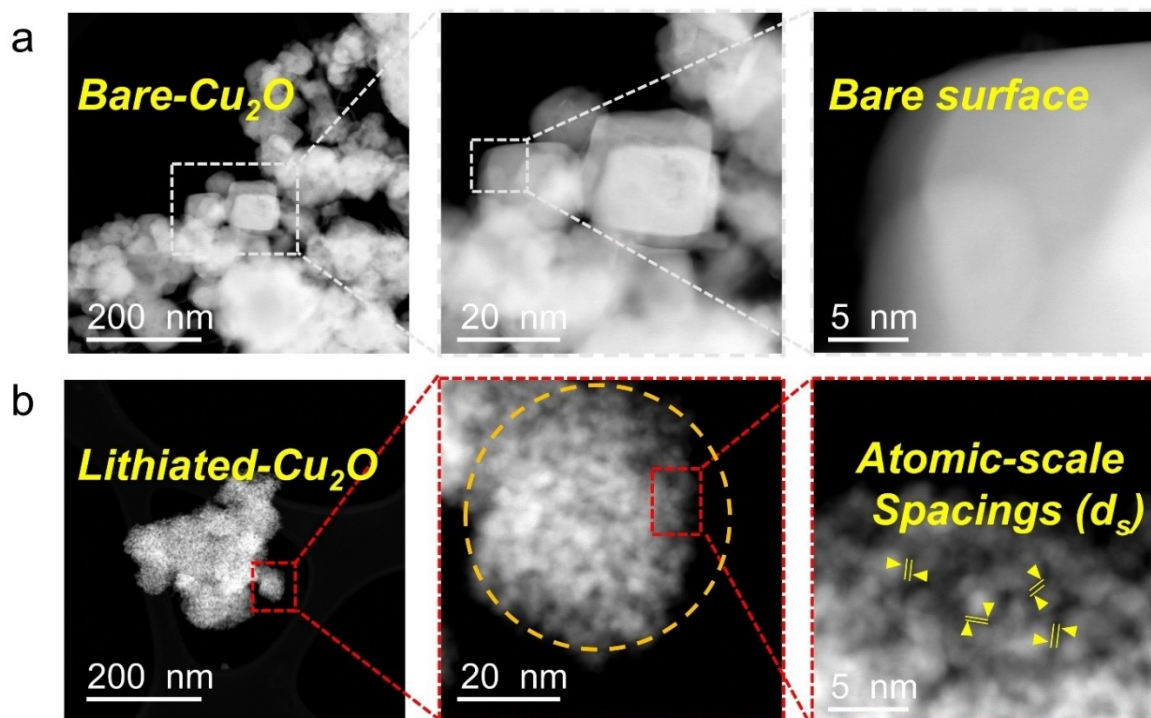
Fig. S6. Scanning transmission electron microscopy (STEM) analysis of Cu₂O. (**a**) STEM images of bare Cu₂O. Enlarged images from low to high magnification were pointed with white boxes and lines. (**b**) STEM images of lithiated Cu₂O (atomic-scale spacings highlighted in an orange circle and yellow parallel lines with points).

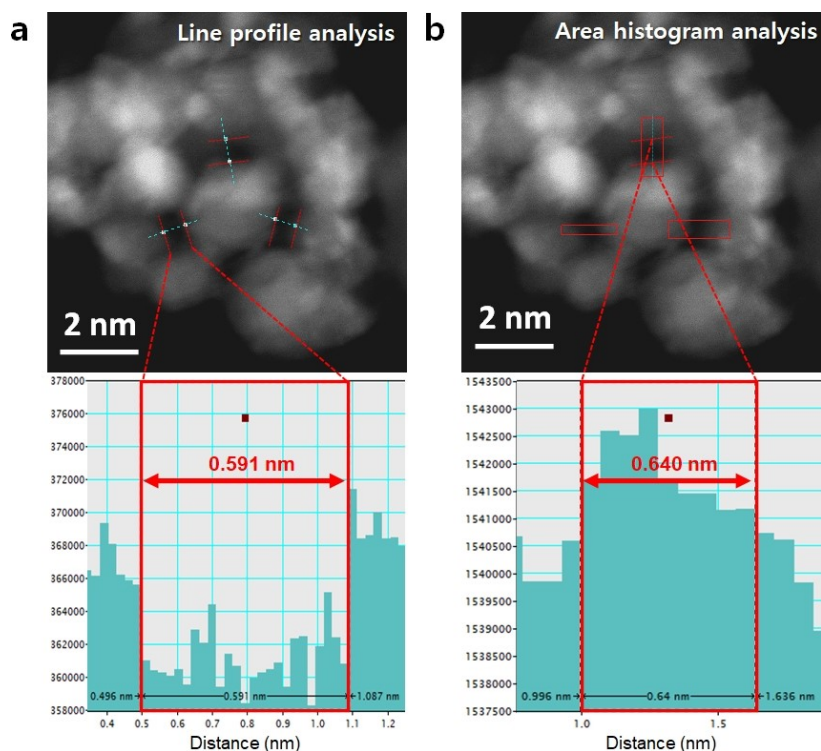**Fig. S7. How to measure sizes of atomic-scale spacings of Cu₂O with d_s samples in STEM images.** Two representatives are demonstrated: a line profile analysis and an area profile analysis. (**a**) Atomic scale spacing measurement in conversion reaction derived Cu₂O nanoparticles. (**b**) Atomic scale spacing measurement double-checked from area histogram pixel analysis to convert into line profile.
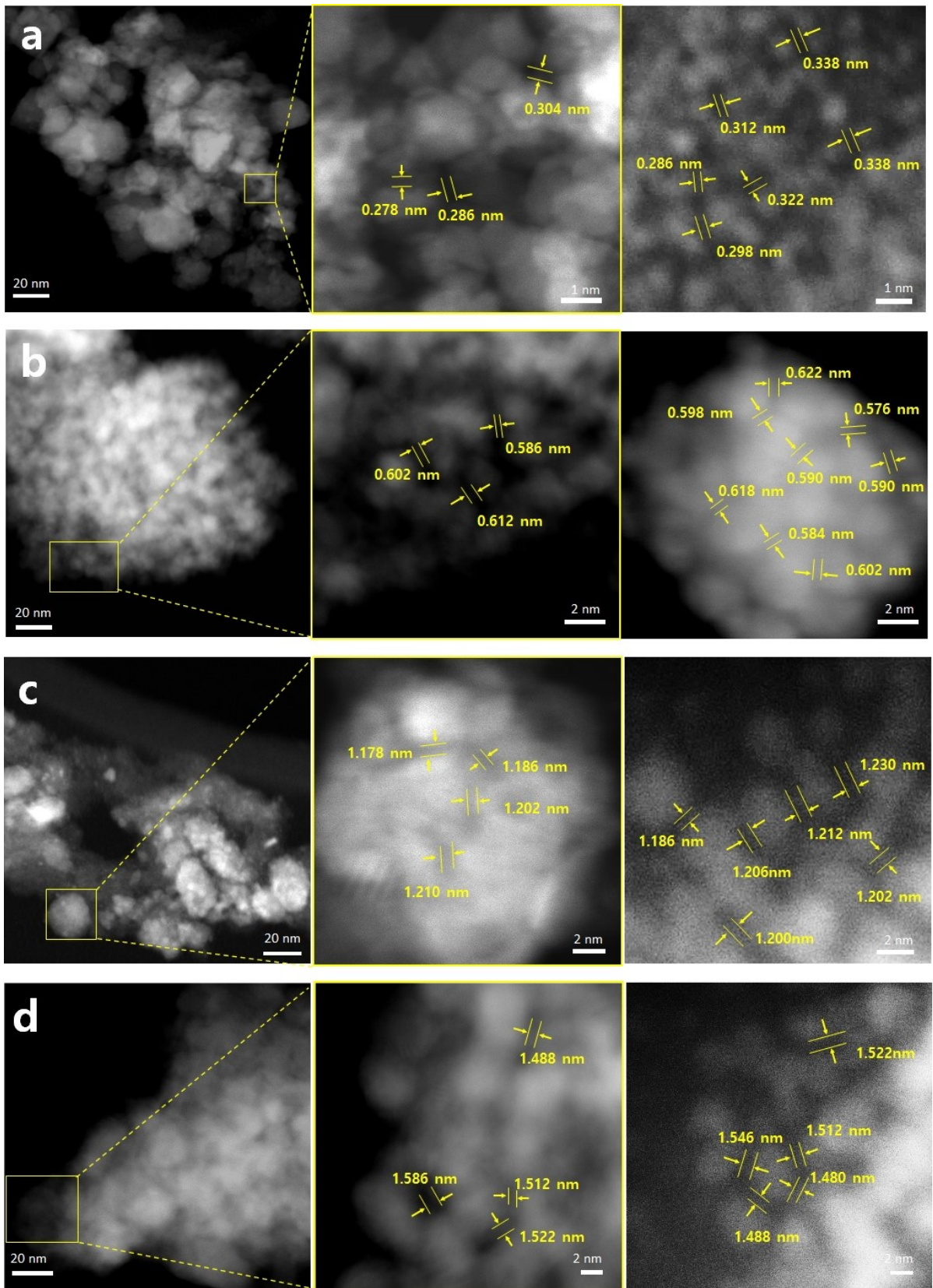
Fig. S8. Distances of 'atomic-scale spacings (d_s)' estimated from STEM images. A line and area profile method (Fig. S6) was used to measure d_s described. (a) Step I, (b) Step II, (c) Step III, and (d) step IV.

	Step I	Step II	Step III	Step IV
N	175	185	217	159
Mean	3.21607	6.00083	12.00276	14.95818
Standard Deviation	0.54605	1.46618	1.29278	1.87768
Standard Error	0.04128	0.1078	0.08776	0.14891
Median	3.05	6.02	12.00	15.00
Notation	3Å-Cu	6Å-Cu	12Å-Cu	15Å-Cu

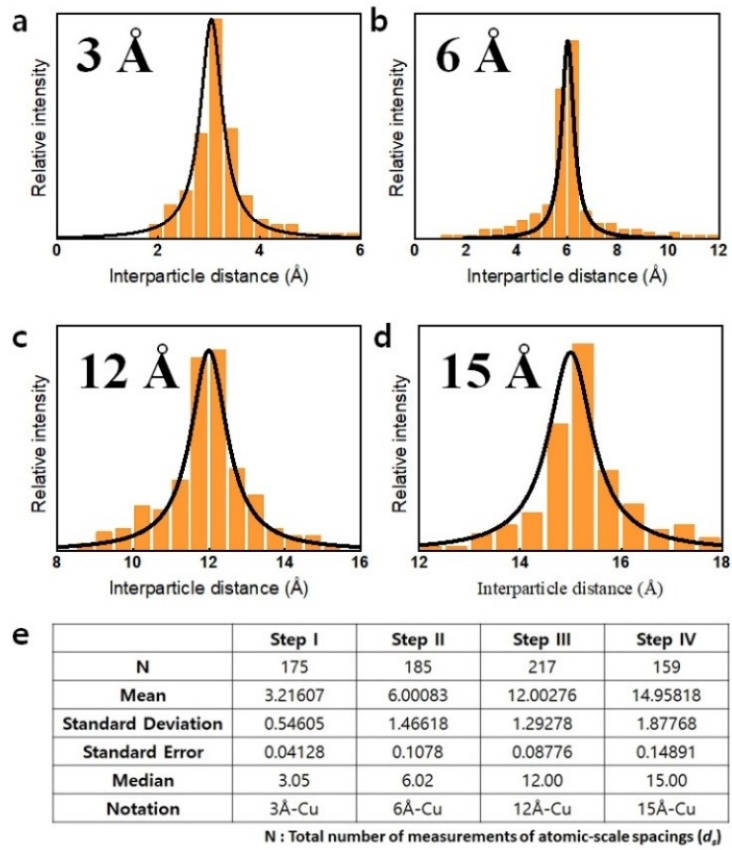N : Total number of measurements of atomic-scale spacings (d_s)

Fig. S9. Statistical distribution of 'atomic-scale spacings (d_s)' measured from STEM images. Statistical distributions were plotted based on the measurement of d_s from STEM images (Fig. S7). (a) Step I, (b) Step II, (c) Step III, and (d) step IV. (e) Also, the results of statistics from a-d were summarized. We conducted a statistical analysis based on the measurement of over 150 d_s for all the samples.
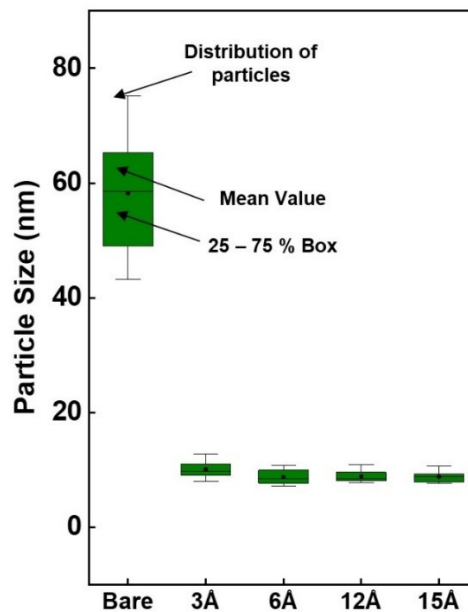
Fig. S10. Particle size distribution from the measurement of TEM images. The average and mean values of particles from bare, 3Å-Cu, 6Å-Cu, 12Å-Cu, and 15Å-Cu were plotted.
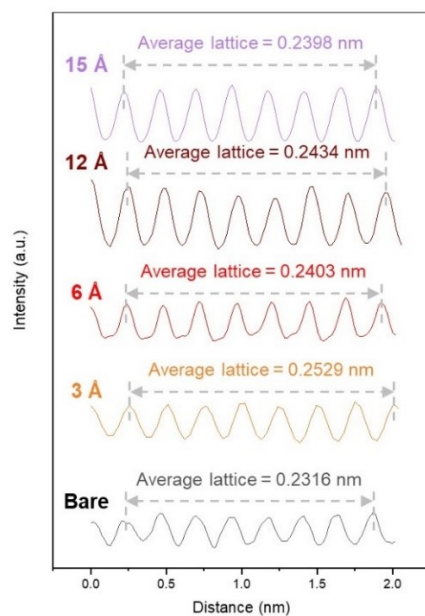
Fig. S11. Intensity profiles along lines vertical to lattice fringes of the TEM images of Cu_2O.
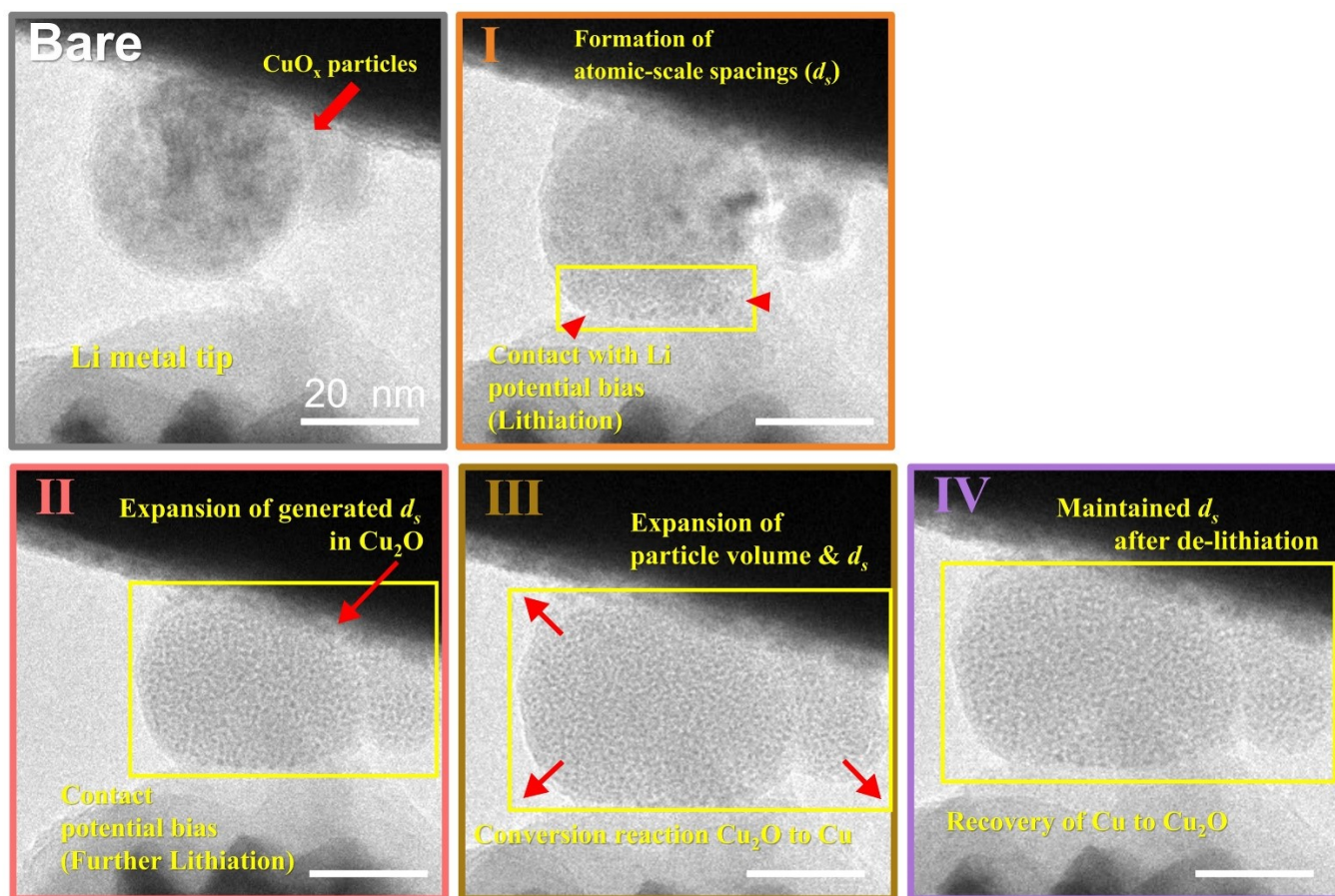
Fig. S12. *in-situ* TEM analysis. Lithiation of Cu_2O was observed with real-time TEM techniques where only two Cu_2O particles are in contact with each other. The detailed process of contact with the Li metal tip is also described.

a Aqueous phase cell

b GDE(Gas diffusion electrode) cell

c
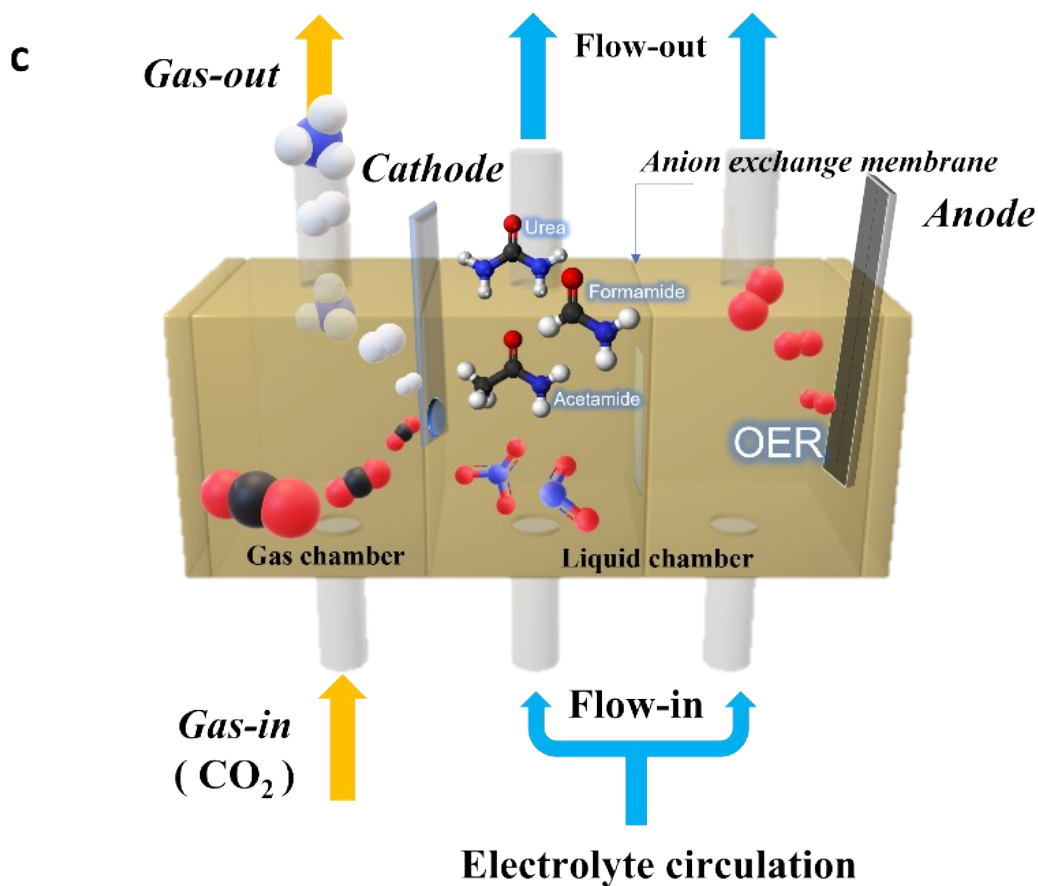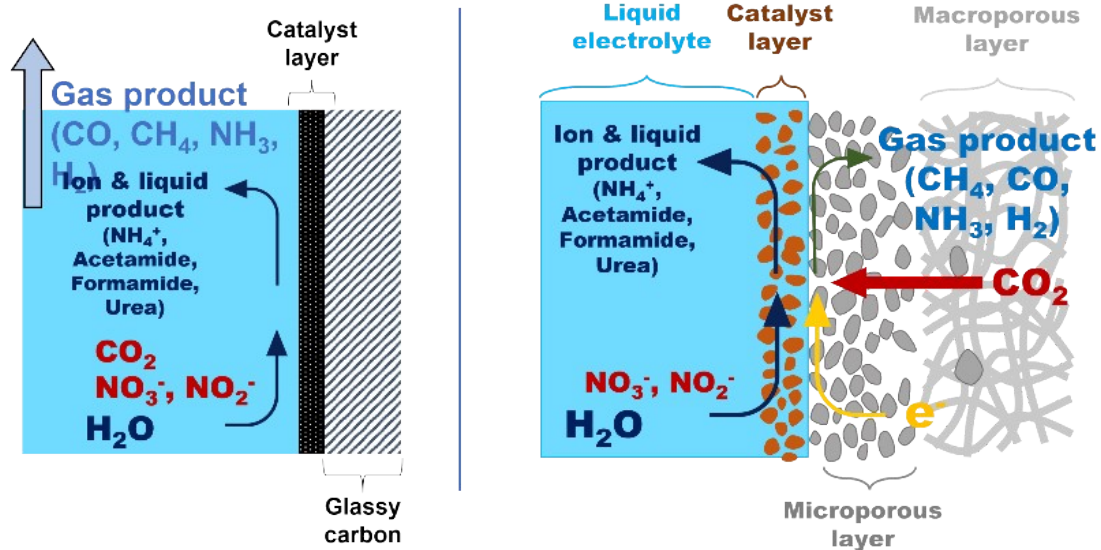
Fig. S13. Comparison of CR-CO_2/NO_3^- in aqueous phase H cell and gas phase GDE cell. (**a**) Aqueous phase H cell. (**b**) Gas phase GDE cell. (**c**) Reaction schemes for GDE cell.
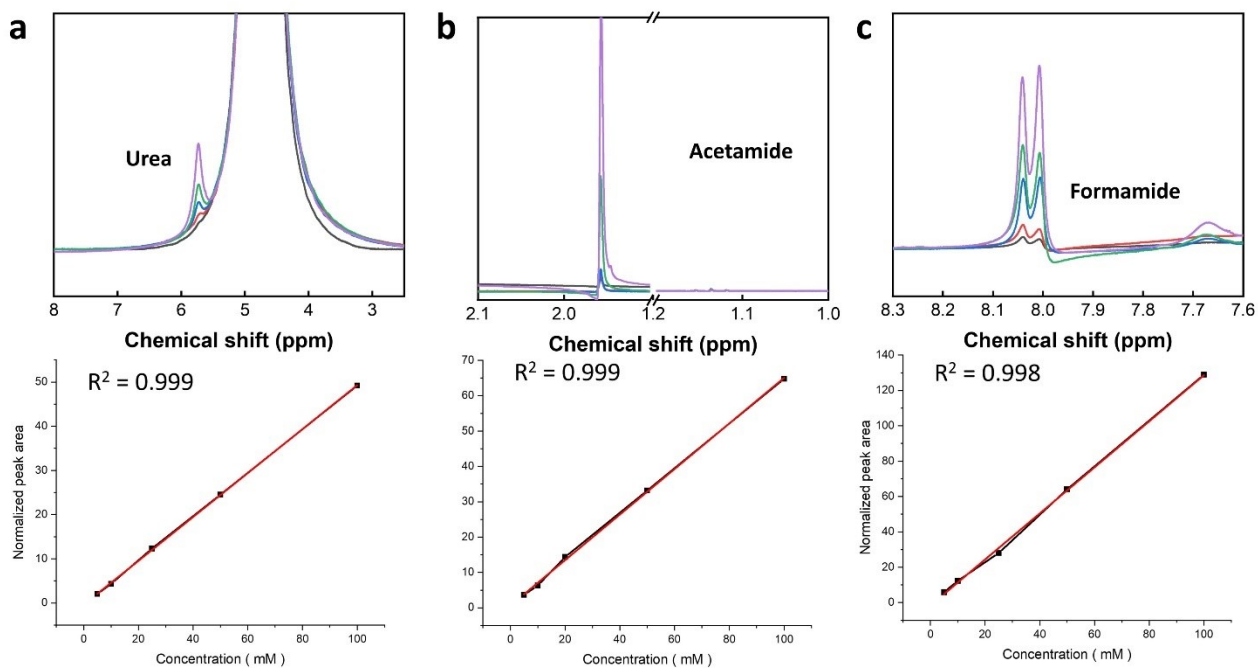
Fig. S14. Calibration data of C-N coupled products (urea, acetamide, and formamide). From the measurement of FT-NMR, each product was calibrated. 5, 10, 25, 50, and 100 mM of analytes were added to an aqueous solution. The peak area of the characteristic peak was used for calibration. (**a**) urea, (**b**) acetamide, and (**c**) formamide.
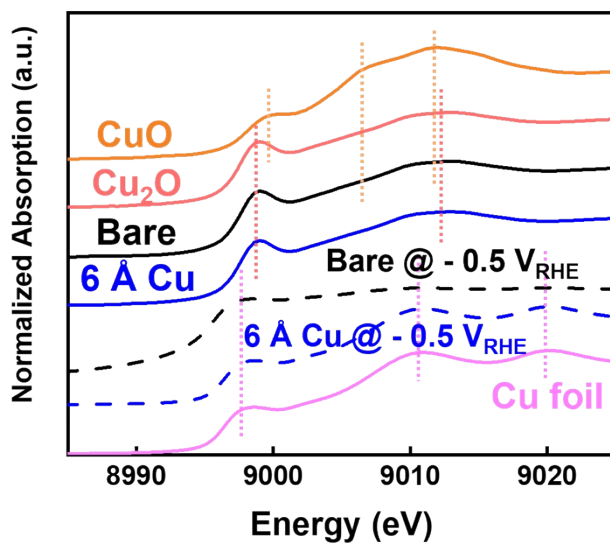
Fig. S15. *In-situ* XANES analysis of bare and 6Å-Cu under the operating condition of CR-CO$_2$/NO$_3^-$. Structural change from Cu$_2$O to metallic Cu was confirmed.
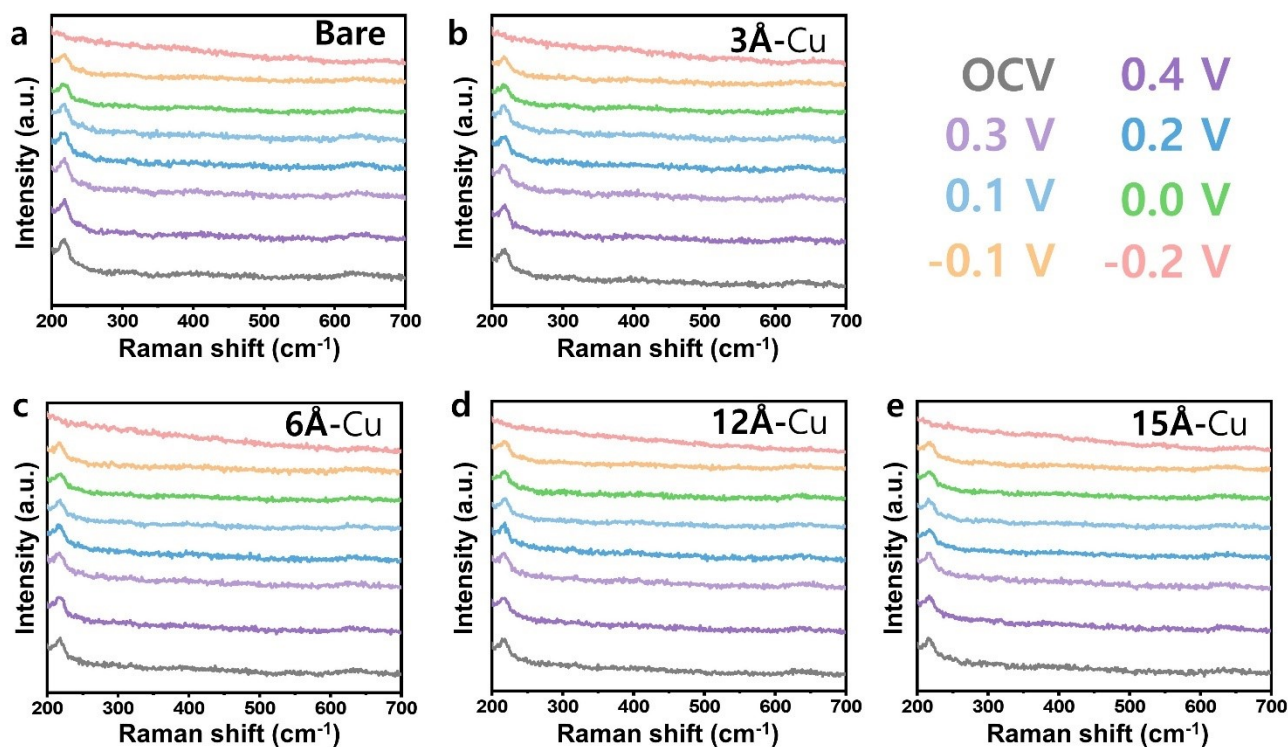
Fig. S16. *In-situ* **Raman spectroscopy measurements** of Cu$_2$O sisters. From the open-circuit-voltage (OCV) and 0.4 V$_{RHE}$, negative reduction potential was applied while Raman spectroscopy was measured. (**a**) Bare, (**b**) 3Å-Cu, (**c**) 6Å-Cu, (**d**) 12Å-Cu, and (**e**) 15Å-Cu. All the samples showed conversion of Cu$_2$O into metallic Cu under cathodic polarization.
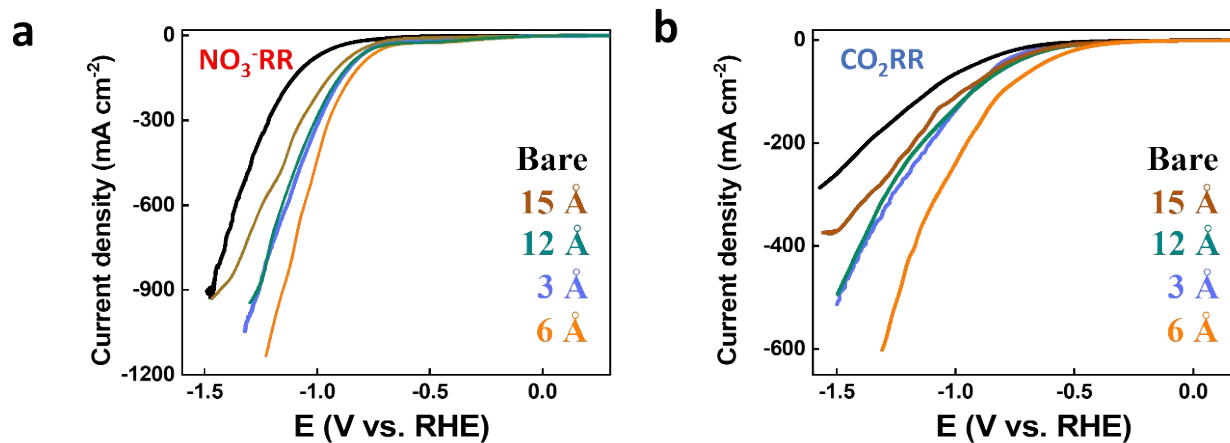
Fig. S17. Electrochemical NO$_3^-$RR and CO$_2$RR. Linear sweep voltammetry was conducted to investigate the electrochemical performance of each reaction. LSVs were performed with a scan rate of 10 mV s^{-1}. (**a**) NO$_3^-$RR and (**b**) CO$_2$RR.
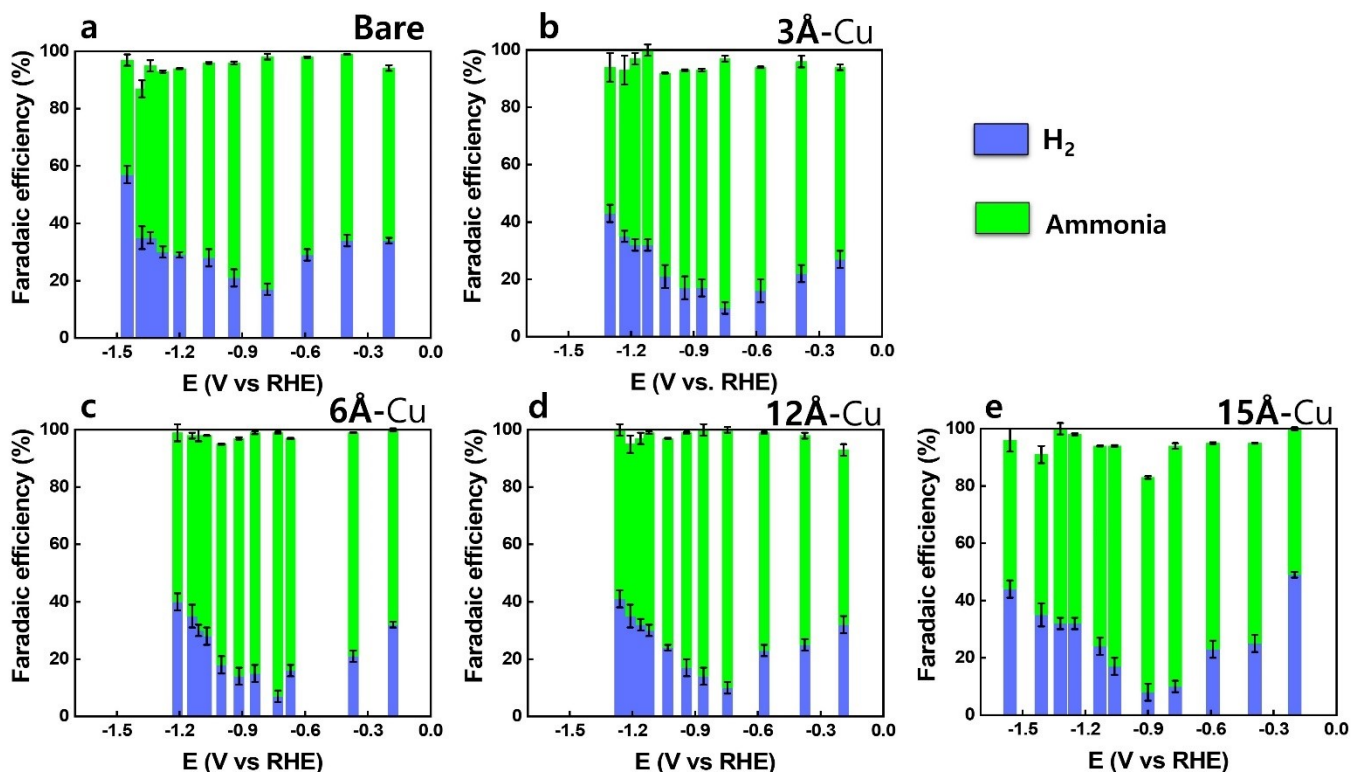
Fig. S18. Product analysis of NO₃⁻RR. Depending on d_s, synthesized ammonia and hydrogen Faradaic efficiencies are described depending on applied potentials. (**a**) Bare, (**b**) 3Å-Cu, (**c**) 6Å-Cu, (**d**) 12Å-Cu, and (**e**) 15Å-Cu.
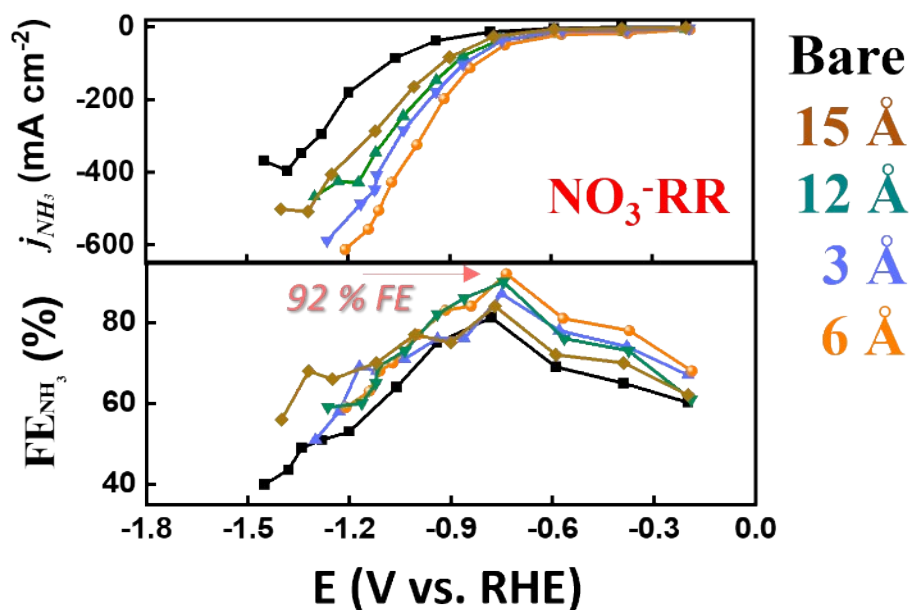
Fig. S19. Electrochemical NO₃⁻ reduction reaction (NO₃⁻RR). Chronopotentiometry (CP) induced ammonia partial current density (j_{NH3}) and ammonia Faradaic efficiency (FE$_{NH3}$) according to applied potentials. As we used an alkaline electrolyte, therefore, the released ammonia was trapped in a 1 M hydrochloric acid solution.
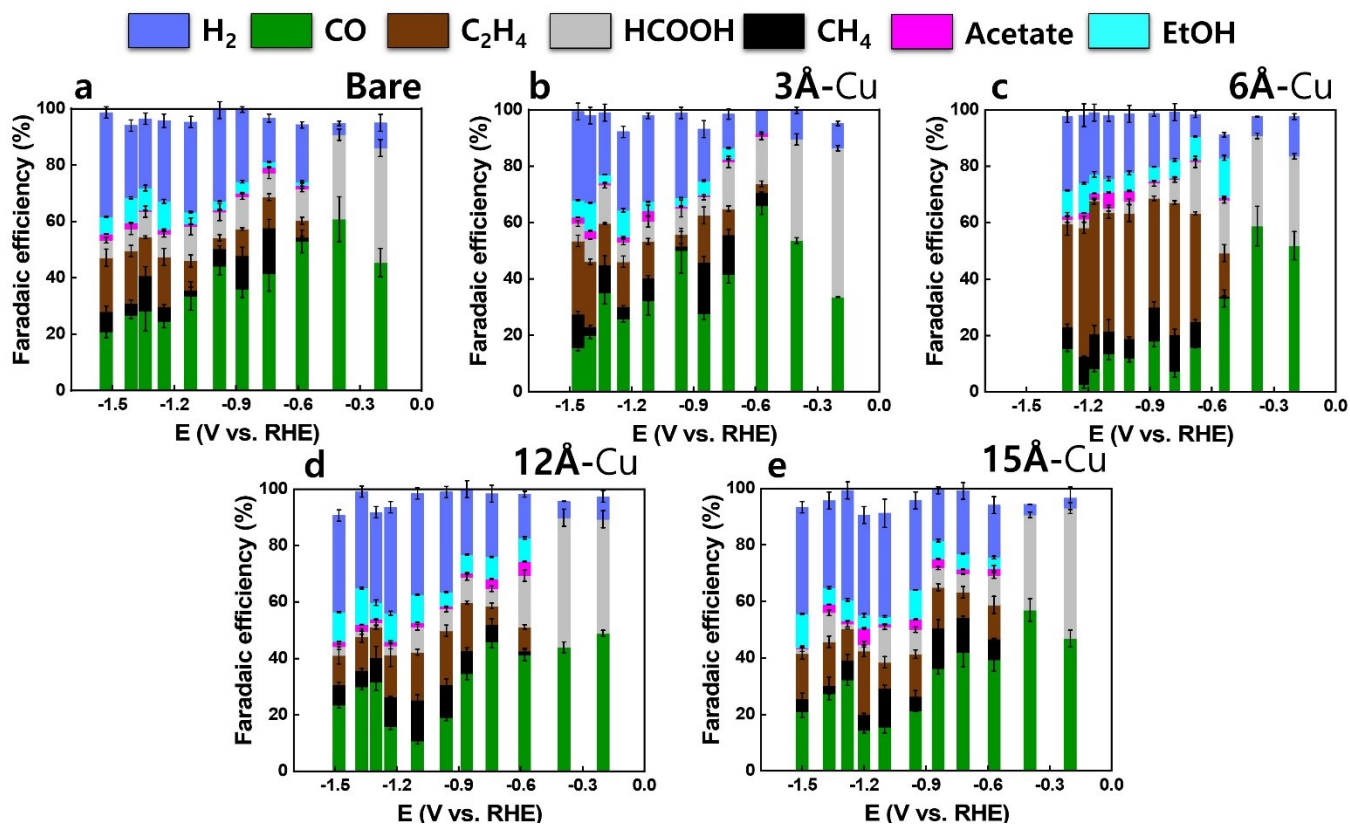
Fig. S20. Product analysis of CO₂RR. Depending on d_s, synthesized CO_2RR products' Faradaic efficiencies are described depending on applied potentials. (**a**) Bare, (**b**) 3Å-Cu, (**c**) 6Å-Cu, (**d**) 12Å-Cu, and (**e**) 15Å-Cu.
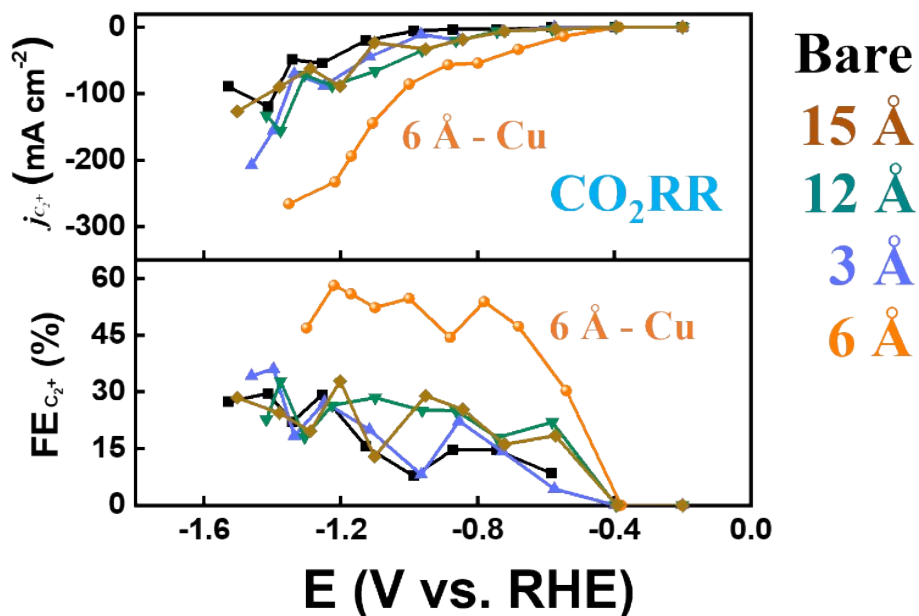
Fig. S21. Electrochemical CO₂ reduction reaction (CO₂RR). Chronopotentiometry (CP) induced C_{2+} partial current density (j_{C2+}) and C_{2+} Faradaic efficiency (FE_{C2+}) according to applied potentials.
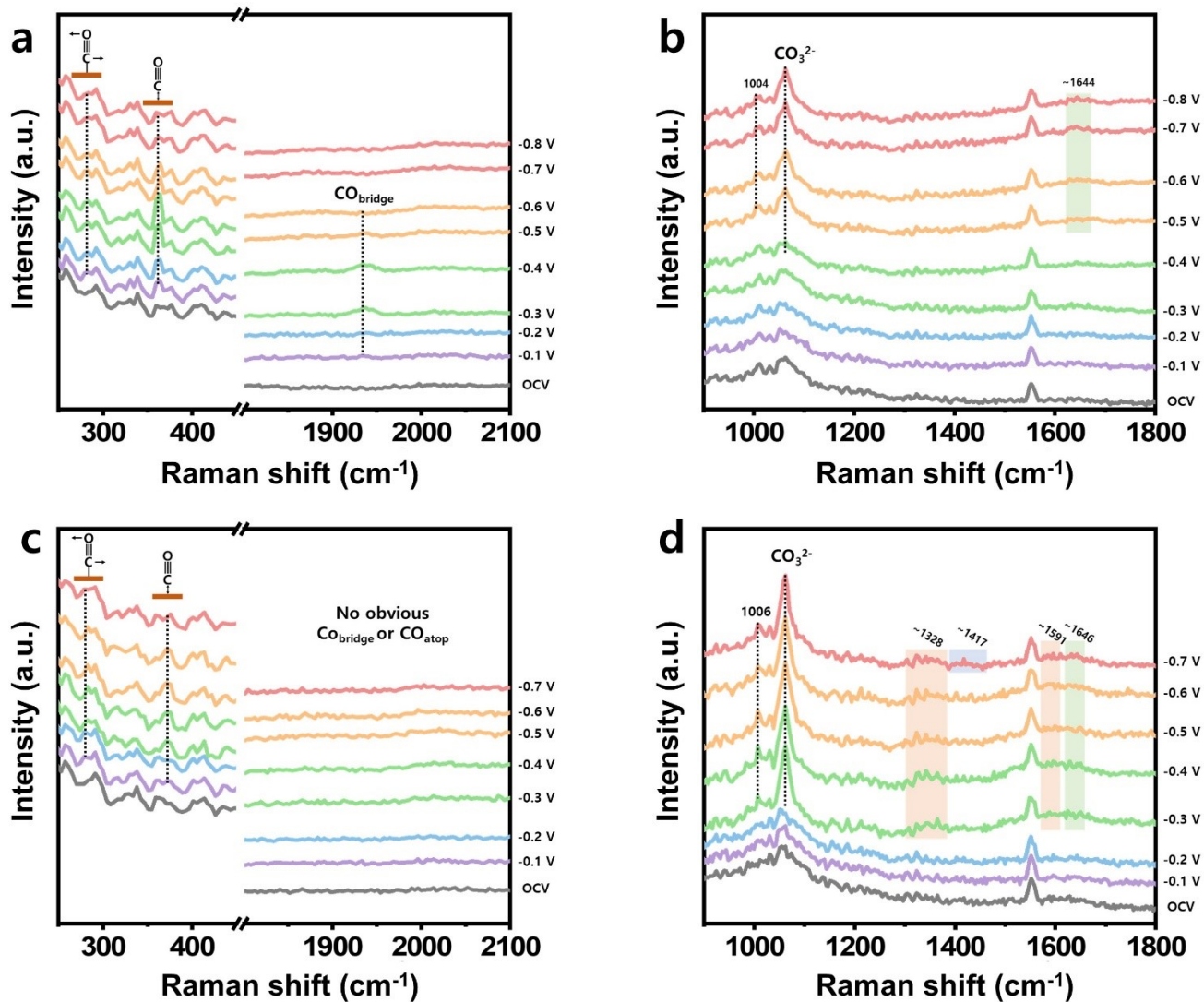
Fig. S22. *In-situ* **Raman spectra of different catalysts under different applied potentials during CR-CO$_2$/NO$_3^-$.** Raman spectra of bare Cu$_2$O at (**a**) CO region and (**b**) C-N coupling region. Raman spectra of 6Å-Cu at (**c**) CO region and (**d**) C-N coupling region.
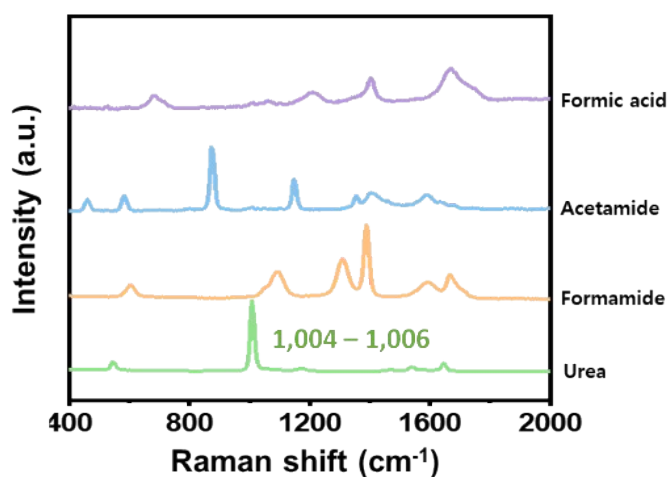
Fig. S23. Reference Raman spectra of possible liquid products.
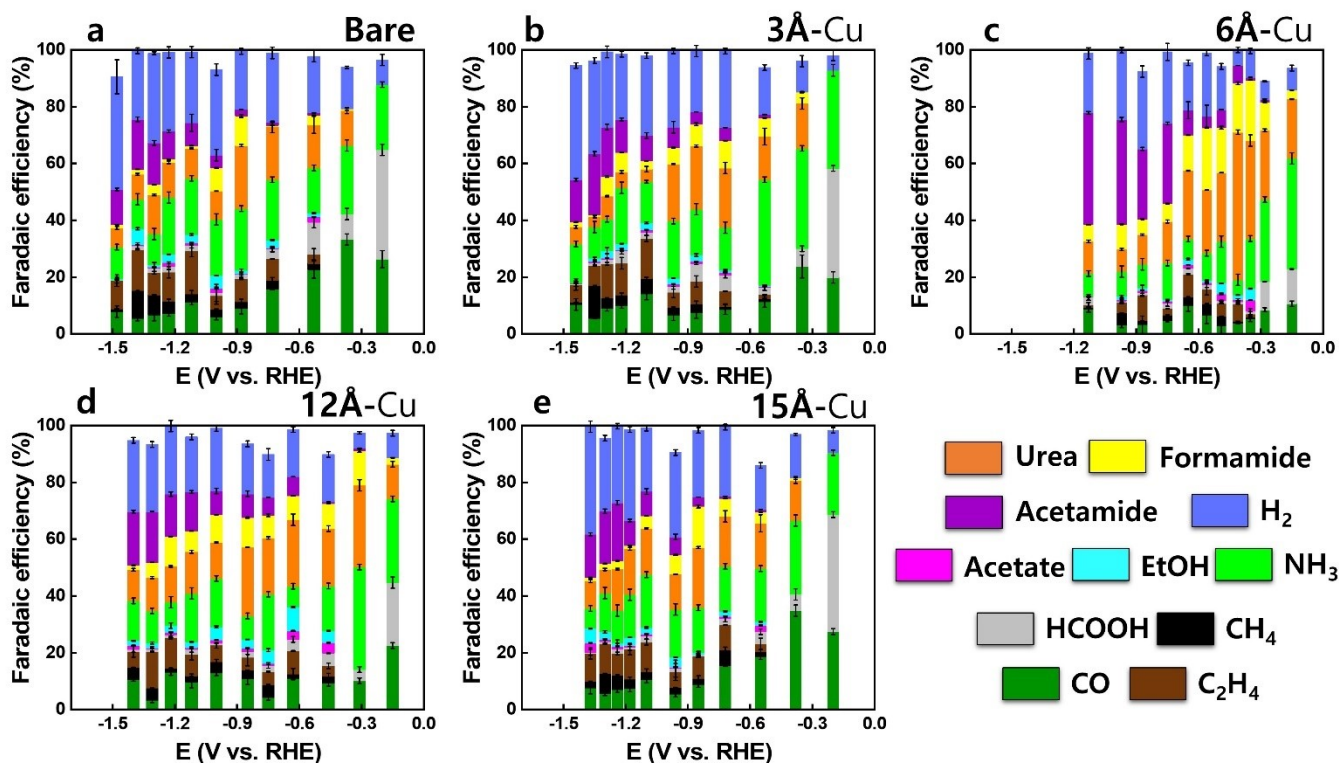
Fig. S24. Product analysis of CR-CO$_2$/NO$_3^-$. Depending on d_s, synthesized CR-CO$_2$/NO$_3^-$ products' Faradaic efficiencies are described depending on applied potentials. (**a**) Bare, (**b**) 3Å-Cu, (**c**) 6Å-Cu, (**d**) 12Å-Cu, and (**e**) 15Å-Cu.
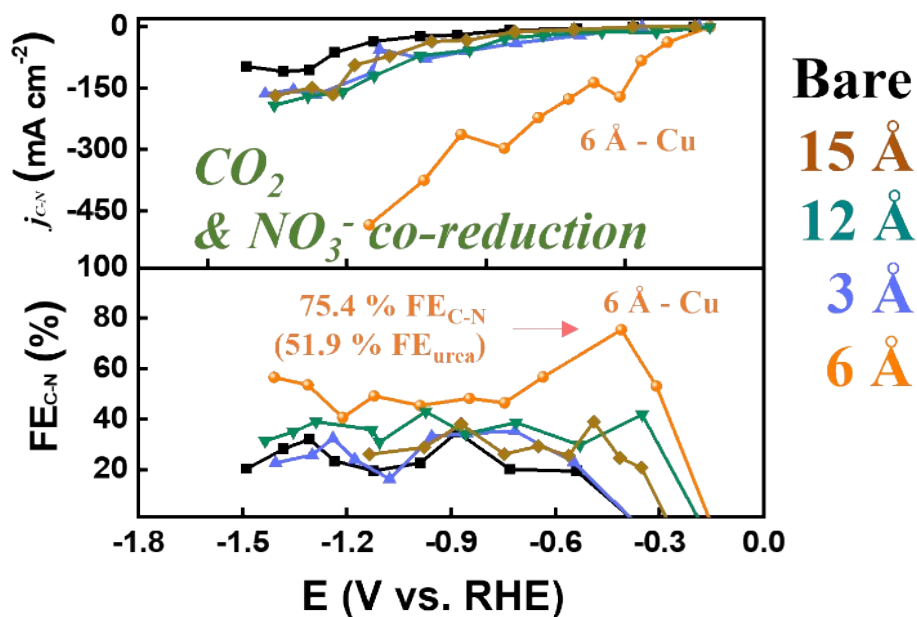
Fig. S25. Electrochemical CO$_2$ and NO$_3^-$ co-reduction reaction (CR-CO$_2$/NO$_3^-$). Chronopotentiometry (CP) induced C-N products partial current density (j_{C-N}) and C-N Faradaic efficiency (FE$_{C-N}$) according to applied potentials.
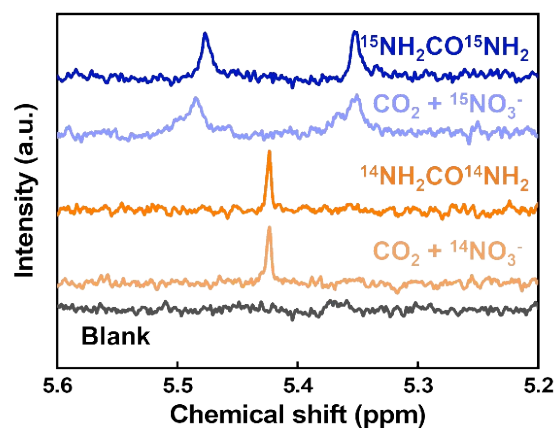
Fig. S26. Isotope experiment. ^{1}H NMR spectra of electrolyte after the chronopotentiometry experiment of CO_2 + ${}^{14}NO_3^-$ / CO_2 + ${}^{15}NO_3^-$ and standard ^{14}N-urea / ^{15}N-urea solution. Comparison of standard solution and experimental products gives evidence of urea synthesis from CO_2 and NO_3^- without the effect of impurities.
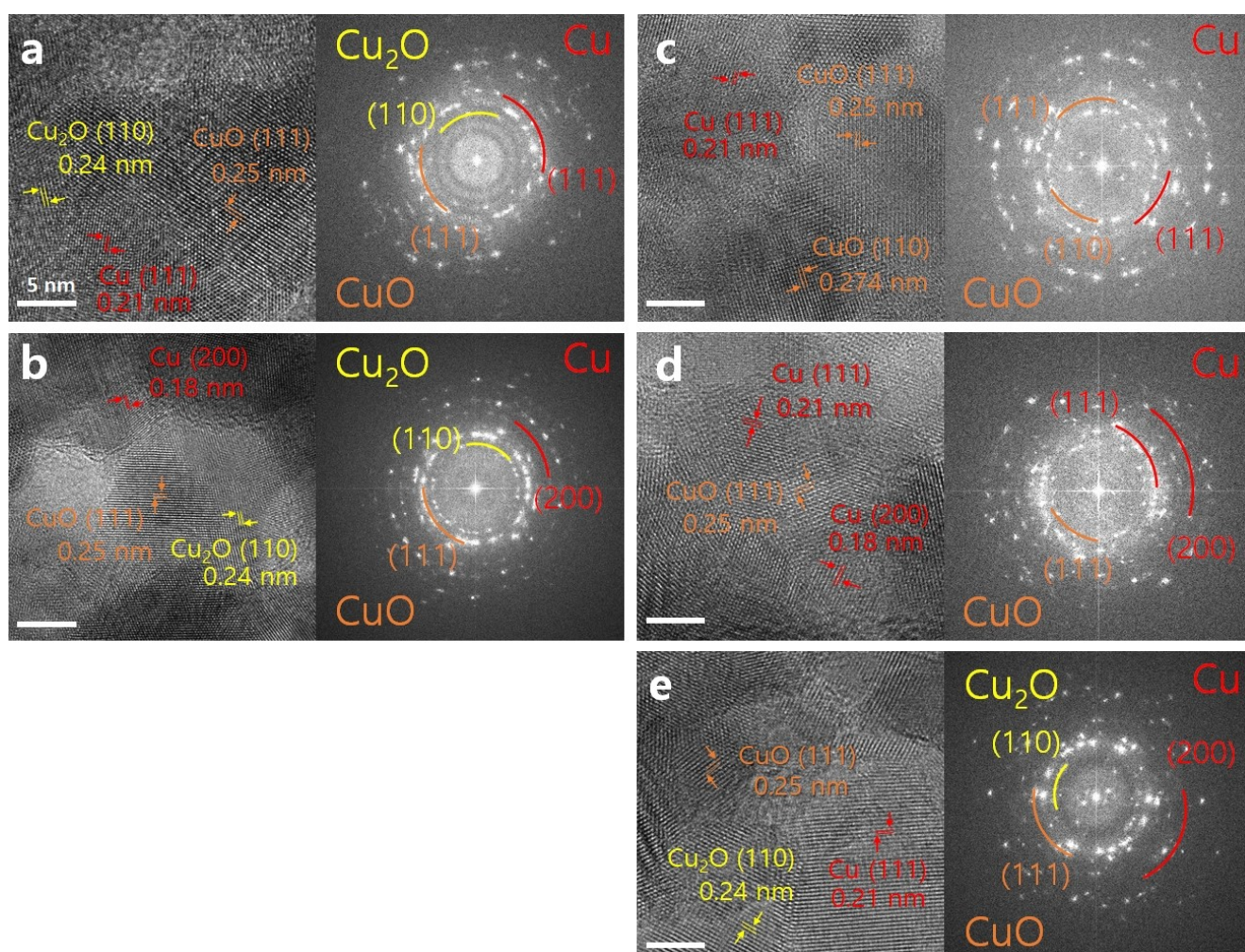
Fig. S27. HR-TEM images with FFT analysis after electrocatalysis. Lattices and facets were analysed on TEM images with an inset of FFT. (**a**) Bare, (**b**) 3Å-Cu, (**c**) 6Å-Cu, (**d**) 12Å-Cu, and (**e**) 15Å-Cu. We note that all the samples including bare Cu_2O are measured after 1 h of CR-CO_2/NO_3^-.
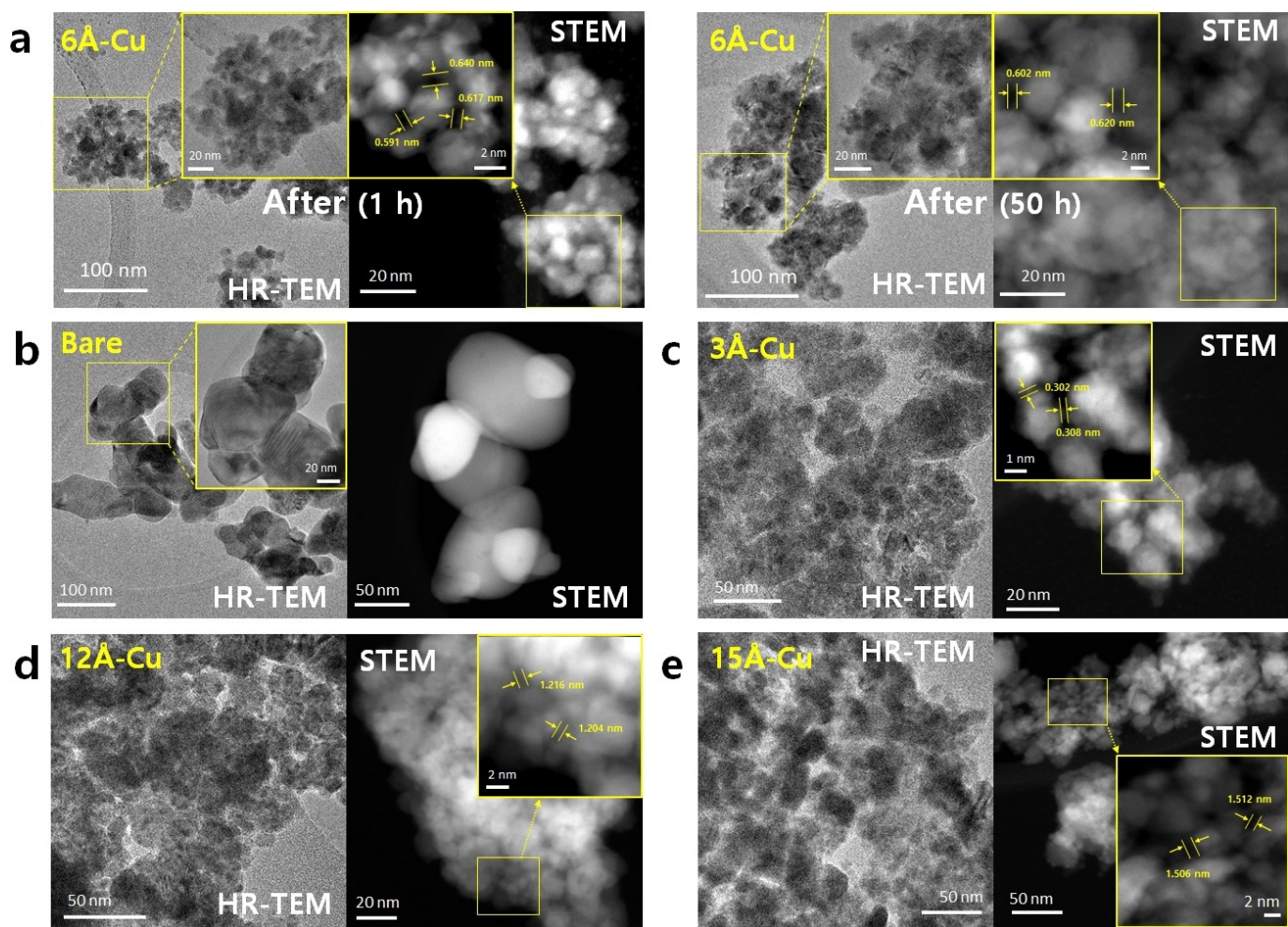
Fig. S28. Morphology and atomic-scale spacings (d_s) from HR-TEM and STEM images after electrocatalysis. (**a**) 6Å-Cu after 1 h CR-CO_2/NO_3^- (left side of images) and after 50 h CR-CO_2/NO_3^- (right side of images), (**b**) bare after 1 h CR-CO_2/NO_3^-, (**c**) 3Å-Cu after 1 h CR-CO_2/NO_3^-, (**d**) 12Å-Cu after 1 h CR-CO_2/NO_3^-, and (**e**) 15Å-Cu after 1 h CR-CO_2/NO_3^-. The HR-TEM and STEM images show that the morphology and the atomic-scale spacings of the lithiated/de-lithiated Cu catalysts were maintained after the electrochemical CR-CO_2/NO_3^-.
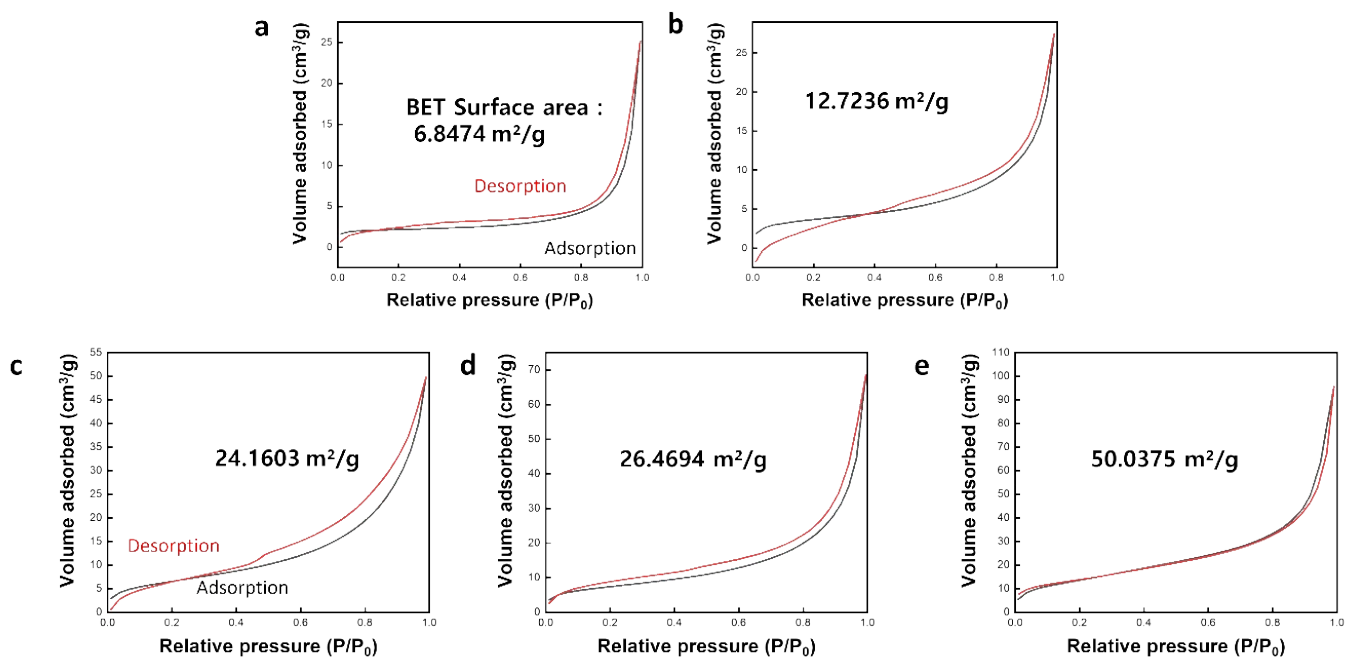
Fig. S29. BET surface area comparison. Specific BET surface area values were obtained. Adsorption and desorption profiles of each sample. (**a**) Bare, (**b**) 3Å-Cu, (**c**) 6Å-Cu, (**d**) 12Å-Cu, and (**e**) 15Å-Cu.
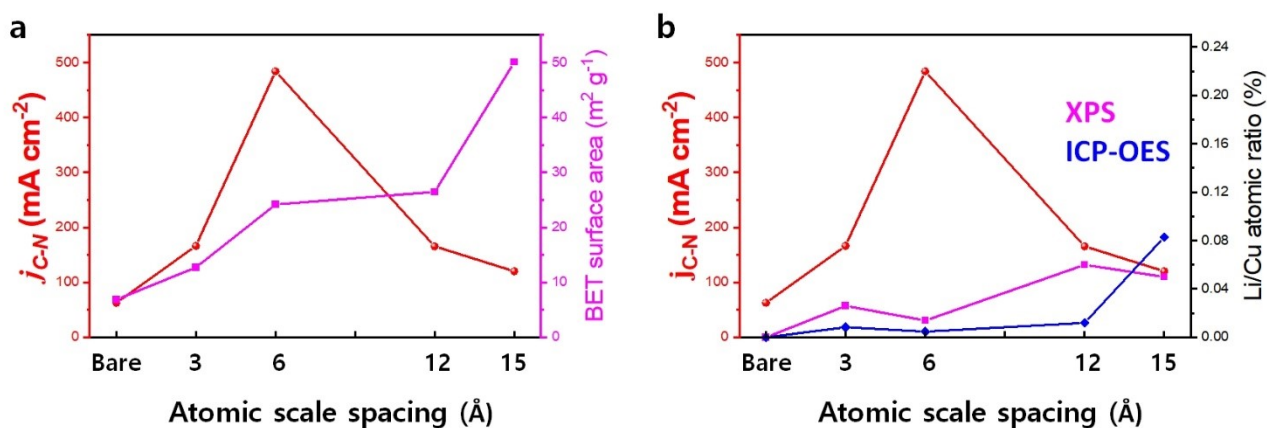
Fig. S30. Comparison of catalytic activity with specific surface area (a), Li/Cu ratio (b) as a function of d_s. The partial current density of C-N coupling is not consistent with the effects of specific BET surface area and residual lithium contents.
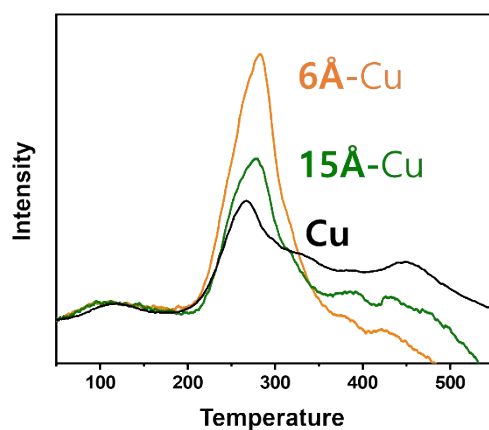
Fig. S31. CO$_2$ temperature programmed desorption (CO$_2$-TPD) results. CO$_2$-TPD of 6Å-, 15Å-Cu and Cu reference was measured.
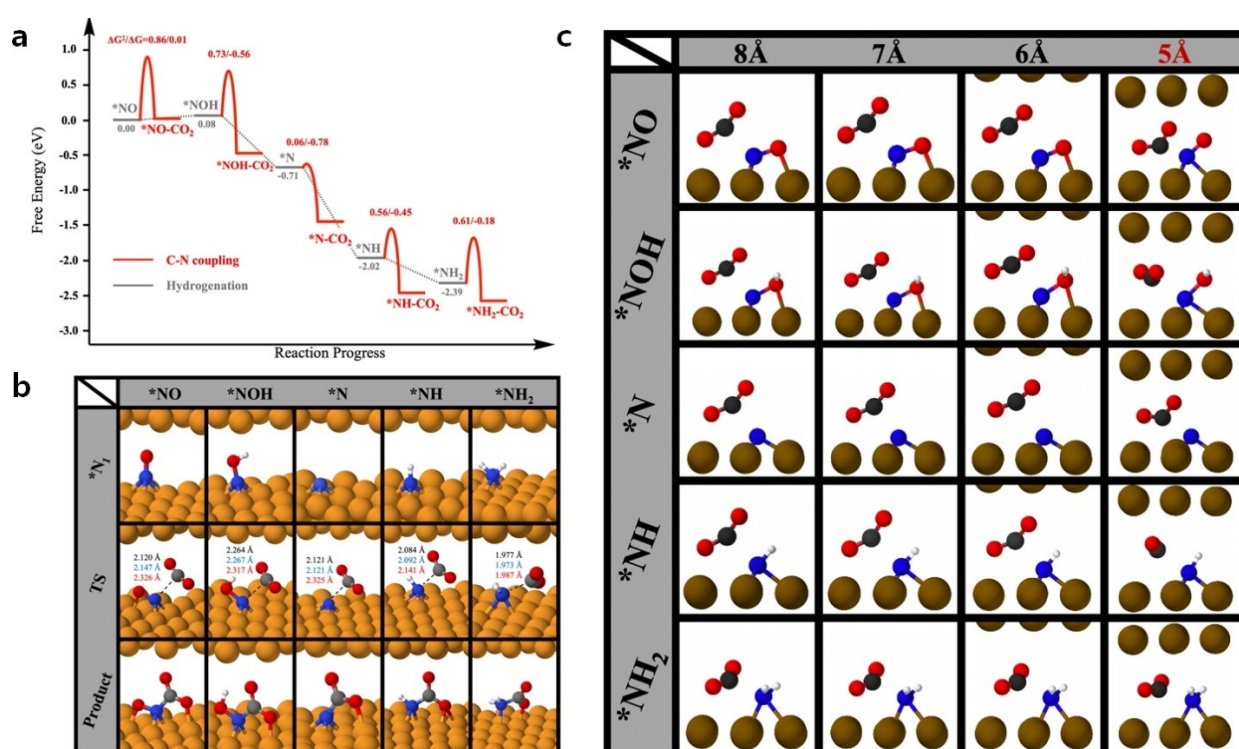
Fig. S32. (**a**) The energetics of *N$_1$ hydrogenation by proton-electron pairs and its coupling reactions with CO$_2$ at U = 0.0 V$_{SHE}$ and pH = 0; (**b**) reduction of *NO to *NOH, *N, *NH, and *NH$_2$, and the formation of C-N coupling transition states and products through *N$_1$ intermediates reacting with CO$_2$. During the transition states, a C-N bond is being formed, and the bond lengths at ds of 8, 7, and 6 Å are denoted and visually distinguished by black, blue, and red colors. (c) The transition state structures of C-N formation through the coupling of *N$_1$ intermediates with CO$_2$ at different d_s.

Table S1. Atomic composition of samples and Li/Cu ratio from XPS measurements

XPS	Composition (atomic %)		Li/Cu atomic ratio
Bare	Cu	62.72	0
	Li	-	
	O	35.13	
Step I (3Å-Cu)	Cu	48.11	0.026
	Li	1.26	
	O	43.08	
Step II (6Å-Cu)	Cu	49.11	0.014
	Li	0.68	
	O	43.58	
Step III (12Å-Cu)	Cu	42.59	0.060
	Li	2.56	
	O	45.94	
Step IV (15Å-Cu)	Cu	47.89	0.050
	Li	2.40	
	O	49.06	

Table S2. Atomic composition of samples and Li/Cu ratio from ICP-OES measurements

ICP-OES	Composition (ppm)		Li/Cu atomic ratio
Bare	Cu	893,429	0
	Li	-	
Step I (3Å-Cu)	Cu	807,884	0.0084
	Li	7.40	
Step II (6Å-Cu)	Cu	783,831	0.0048
	Li	4.07	
Step III (12Å-Cu)	Cu	817,324	0.012
	Li	10.3	
Step IV (15Å-Cu)	Cu	800,042	0.083
	Li	7.28	

Table S3. Comparison of electrochemical C-N coupling electrocatalysts

Catalyst	Media	FE (%)	Partial current density (mA cm^{-2})	Urea yield rate	Stability (h)	Ref.
$CO_2 + NO_3^-$						
Cu with atomic-scale spacings	**1 M KOH**	**51.9**	**115.25**	**7,541.9 µg h^{-1} mg$_{cat}$$^{-1}$**	**50**	**This work**
Zn	0.2 M KHCO$_3$	35	-	15.13 mmol h^{-1} g^{-1}	-	(1)
Ni-Pc	0.2 M KHCO$_3$	41	11	-	-	(2)
TiO$_2$/Nafion	0.1 M KNO$_3$	40	0.8	0.33 µmol h^{-1}	2	(3)
In(OH)$_3$	0.1 M KHCO$_3$	53.4	0.3	533.1 µg h^{-1} mg$_{cat}$$^{-1}$	12	(4)
XC72R-AuPd	0.025 M KNO$_3$ + 0.075 M KHCO$_3$	15.6	3 (estimated)	204.2 µg h^{-1} mg$_{cat}$$^{-1}$	10 cycles	(5)
Cu-N-C catalysts	0.1 M KHCO$_3$	28	27	1800 µg h^{-1} mg$_{cat}$$^{-1}$	12	(6)
FeNi-DASC	0.1 M KHCO$_3$	17.8	8 (estimated)	20.2 mmol h^{-1} g$_{cat.}$$^{-1}$	5	(7)
PdCu/CBC	0.05 M KNO$_3$	69.1	2.8 (estimated)	763.8 µg h^{-1} mg$_{cat}$$^{-1}$	10	(8)
$CO_2 + NO_2^-$						
Cu-TiO$_2$	0.2 M KHCO$_3$	43.1	- 3.448 (estimated)	20 µmol h^{-1}	2	(9)
Te-Pd NCs	0.05 M KNO$_2$	12.2	0.276 (estimated)	-	5	(10)
ZnO-V	0.2 M NaHCO$_3$ + 0.1 M NaNO$_2$	23.26	6.978 (estimated)	16.56 µmol h^{-1}	5 cycle	(11)
$CO_2 + N_2$						
PPy-coated Pt	0.1 M Li$_2$SO$_4$ +	7.1	-	21.2 µmol (5 h)	5	(12)

	0.03 M H$^+$					
Pd$_1$Cu$_1$/TiO$_2$-400	0.1 M KHCO$_3$	8.92	-	3.36 mmol h^{-1} g^{-1}	12	(13)
Bi/BiVO$_4$	0.1 M KHCO$_3$	12.55	0.5 (estimated)	5.91 mmol h^{-1} g^{-1}	10	(14)
BiFeO$_3$/BiVO$_4$	0.1 M KHCO$_3$	17.18	3.1 (estimated)	4.94 mmol h^{-1} g^{-1}	10	(15)
Ni(BO$_3$)$_2$	0.1 M KHCO$_3$	20.36	2.44	9.70 mmol h^{-1} g^{-1}	2	(16)
InOOH	0.1 M KHCO$_3$	20.97	-	6.85 mmol h^{-1} g^{-1}	-	(17)

Table S4. Free energy barriers and reaction free energies (in parentheses) for 15 C–N coupling reactions (the unit is eV)

	*NO	*NOH	*N	*NH	*NH$_2$
			Coupling with CO$_{2(g)}$		
d = 5.0 Å	0.87 (-0.40)	0.96 (-0.73)	0.29 (-1.88)	0.93 (-0.62)	0.76 (-0.19)
d = 6.0 Å	0.86 (0.01)	0.73 (-0.56)	0.06 (-0.78)	0.56 (-0.45)	0.61 (-0.18)
d = 7.0 Å	0.90 (0.48)	0.67 (-0.26)	0.19 (-0.34)	0.66 (-0.10)	0.70 (0.05)
d = 8.0 Å	1.00 (0.62)	0.75 (-0.17)	0.29 (-0.18)	0.75 (0.00)	0.77 (0.14)
bare	1.07 (0.84)	0.79 (-0.06)	0.60 (0.00)	0.81 (0.11)	0.78 (0.25)
			*Coupling with *COOH*		
d = 5.0 Å	0.86 (-0.21)	0.85 (0.45)	0.47 (-1.10)	0.93 (-0.17)	0.92 (-0.03)
d = 6.0 Å	1.07 (-0.44)	1.04 (-0.51)	0.49 (-1.32)	0.92 (-0.67)	0.99 (-0.30)
d = 7.0 Å	1.13 (-0.56)	1.05 (-0.86)	0.56 (-1.44)	0.99 (-0.91)	1.02 (-0.49)
d = 8.0 Å	1.14 (-0.54)	1.07 (-0.84)	0.56 (-1.39)	1.03 (-0.85)	1.02 (-0.40)
bare	1.12 (-0.47)	1.04 (-0.75)	0.65 (-1.27)	1.09 (-0.62)	0.99 (-0.30)
			*Coupling with *CO*		
d = 5.0 Å	0.85 (-0.09)	0.85 (0.36)	0.69 (-1.18)	0.94 (-0.27)	1.03 (0.52)
d = 6.0 Å	0.99 (0.92)	0.85 (0.26)	0.69 (-1.36)	0.96 (0.40)	0.96 (0.27)
d = 7.0 Å	1.12 (1.10)	0.80 (0.28)	0.73 (-1.35)	1.00 (0.52)	0.94 (0.27)

d = 8.0 Å	1.15 (0.90)	0.80 (0.33)	0.74 (-1.30)	1.00 (0.53)	0.96 (0.33)
bare	1.18 (1.19)	0.80 (0.22)	0.77 (-1.23)	1.01 (0.53)	0.94 (0.36)

Table S5. Free energies for all calculated species at different atomic spacings

Species	E_{elect}	Thermo	G (eV)
Cu(111)_5Å	-207.5139	0.0000	-207.5139
Cu(111)_6Å	-206.9274	0.0000	-206.9274
Cu(111)_7Å	-206.6909	0.0000	-206.6909
Cu(111)_8Å	-206.5698	0.0000	-206.5698
Cu(111)_bare	-103.1835	0.0000	-103.1835
Cu_CO_5Å	-223.6380	0.1115	-223.5265
Cu_CO_6Å	-223.1768	0.1116	-223.0652
Cu_CO_7Å	-222.9100	0.1106	-222.7994
Cu_CO_8Å	-222.7590	0.1114	-222.6476
Cu_CO_bare	-119.3388	0.1049	-119.2339
Cu_COOH_5Å	-234.4579	0.4830	-233.9749
Cu_COOH_6Å	-233.8338	0.4468	-233.3870
Cu_COOH_7Å	-233.4803	0.4790	-233.0013
Cu_COOH_8Å	-233.3011	0.4868	-232.8143
Cu_COOH_bare	-129.8820	0.4974	-129.3846
Cu_NO_5Å	-221.6857	0.0979	-221.5878
Cu_NO_6Å	-221.0828	0.1037	-220.9791

Cu_NO_7Å	-220.8394	0.1053	-220.7341
Cu_NO_8Å	-220.6957	0.1066	-220.5891
Cu_NO_bare	-117.2793	0.1060	-117.1733
Cu_NOH_5Å	-225.2215	0.3509	-224.8706
Cu_NOH_6Å	-224.6540	0.3519	-224.3021
Cu_NOH_7Å	-224.3295	0.3974	-223.9320
Cu_NOH_8Å	-224.1658	0.3894	-223.7764
Cu_NOH_bare	-120.7362	0.3825	-120.3536
Cu_N_5Å	-214.9030	0.0745	-214.8285
Cu_N_6Å	-214.3389	0.0761	-214.2628
Cu_N_7Å	-214.1289	0.0770	-214.0518
Cu_N_8Å	-214.0034	0.0772	-213.9262
Cu_N_bare	-110.6066	0.0763	-110.5303
Cu_NH_5Å	-219.9542	0.3609	-219.5933
Cu_NH_6Å	-219.3451	0.3657	-218.9793
Cu_NH_7Å	-219.1176	0.3672	-218.7504
Cu_NH_8Å	-218.9838	0.3670	-218.6167
Cu_NH_bare	-115.5712	0.3631	-115.2082
Cu_NH$_2$_5Å	-224.0270	0.6380	-223.3890
Cu_NH$_2$_6Å	-223.3959	0.6463	-222.7496
Cu_NH$_2$_7Å	-223.0951	0.6493	-222.4457
Cu_NH$_2$_8Å	-222.9485	0.6483	-222.3002
Cu_NH$_2$_bare	-119.5221	0.6457	-118.8764
Cu_NO+CO$_2$_TS_5Å	-244.2500	0.2600	-243.9900
Cu_NO+CO$_2$_TS_6Å	-243.6500	0.2600	-243.3900
Cu_NO+CO$_2$_TS_7Å	-243.3807	0.2800	-243.1000
Cu_NO+CO$_2$_TS_8Å	-243.1514	0.2912	-242.8600
Cu_NO+CO$_2$_TS_bare	-139.6572	0.2933	-139.3639

Cu_NO+COOH_TS_5Å	-247.7700	0.5800	-247.1900
Cu_NO+COOH_TS_6Å	-246.9100	0.5400	-246.3700
Cu_NO+COOH_TS_7Å	-246.4600	0.5539	-245.9100
Cu_NO+COOH_TS_8Å	-246.2500	0.5600	-245.6900
Cu_NO+COOH_TS_bare	-142.8392	0.5862	-142.2530
Cu_NO+CO_TS_5Å	-236.9000	0.1500	-236.7500
Cu_NO+CO_TS_6Å	-236.3100	0.1800	-236.1300
Cu_NO+CO_TS_7Å	-235.9157	0.1982	-235.7200
Cu_NO+CO_TS_8Å	-235.7100	0.1900	-235.5200
Cu_NO+CO_TS_bare	-132.2286	0.1888	-132.0398
Cu_NOH+CO$_2$_TS_5Å	-247.6900	0.5100	-247.1800
Cu_NOH+CO$_2$_TS_6Å	-247.4000	0.5600	-246.8400
Cu_NOH+CO$_2$_TS_7Å	-247.0950	0.5663	-246.5300
Cu_NOH+CO$_2$_TS_8Å	-246.8700	0.5700	-246.3000
Cu_NOH+CO$_2$_TS_bare	-143.3922	0.5584	-142.8339
Cu_NOH+COOH_TS_5Å	-251.3400	0.8600	-250.4800
Cu_NOH+COOH_TS_6Å	-250.5900	0.8600	-249.7200
Cu_NOH+COOH_TS_7Å	-250.0829	0.8991	-249.1800
Cu_NOH+COOH_TS_8Å	-249.8600	0.9100	-248.9500
Cu_NOH+COOH_TS_bare	-146.4111	0.8983	-145.5127
Cu_NOH+CO_TS_5Å	-240.5100	0.4700	-240.0300
Cu_NOH+CO_TS_6Å	-240.1000	0.5200	-239.5900
Cu_NOH+CO_TS_7Å	-239.7598	0.5244	-239.2400
Cu_NOH+CO_TS_8Å	-239.5700	0.5200	-239.0500
Cu_NOH+CO_TS_bare	-136.1247	0.5160	-135.6086
Cu_N+CO$_2$_TS_5Å	-238.0900	0.2800	-237.8100
Cu_N+CO$_2$_TS_6Å	-237.7200	0.2500	-237.4700
Cu_N+CO$_2$_TS_7Å	-237.3850	0.2551	-237.1300

Cu_N+CO$_2$_TS_8Å	-237.1648	0.2581	-236.9100
Cu_N+CO$_2$_TS_bare	-133.4327	0.2332	-133.1995
Cu_N+COOH_TS_5Å	-241.3900	0.5700	-240.8200
Cu_N+COOH_TS_6Å	-240.7700	0.5400	-240.2300
Cu_N+COOH_TS_7Å	-240.3732	0.5773	-239.8000
Cu_N+COOH_TS_8Å	-240.1900	0.5900	-239.6100
Cu_N+COOH_TS_bare	-136.6652	0.5866	-136.0786
Cu_N+CO_TS_5Å	-230.3100	0.1600	-230.1500
Cu_N+CO_TS_6Å	-229.8800	0.1700	-229.7100
Cu_N+CO_TS_7Å	-229.5900	0.1600	-229.4300
Cu_N+CO_TS_8Å	-229.4300	0.1700	-229.2600
Cu_N+CO_TS_bare	-125.9744	0.1659	-125.8084
Cu_NH+CO$_2$_TS_5Å	-242.4300	0.5000	-241.9300
Cu_NH+CO$_2$_TS_6Å	-242.2100	0.5300	-241.6900
Cu_NH+CO$_2$_TS_7Å	-241.8917	0.5336	-241.3600
Cu_NH+CO$_2$_TS_8Å	-241.6800	0.5400	-241.1400
Cu_NH+CO$_2$_TS_bare	-138.2072	0.5420	-137.6653
Cu_NH+COOH_TS_5Å	-245.9500	0.8300	-245.1200
Cu_NH+COOH_TS_6Å	-245.3500	0.8200	-244.5200
Cu_NH+COOH_TS_7Å	-244.9247	0.8557	-244.0700
Cu_NH+COOH_TS_8Å	-244.6900	0.8600	-243.8300
Cu_NH+COOH_TS_bare	-141.1727	0.8525	-140.3202
Cu_NH+CO_TS_5Å	-235.1100	0.4400	-234.6700
Cu_NH+CO_TS_6Å	-234.6100	0.4500	-234.1600
Cu_NH+CO_TS_7Å	-234.3100	0.4500	-233.8600
Cu_NH+CO_TS_8Å	-234.1400	0.4500	-233.6900
Cu_NH+CO_TS_bare	-130.7049	0.4524	-130.2526
Cu_NH$_2$+CO$_2$_TS_5Å	-246.6900	0.7900	-245.9000

Cu_NH$_2$+CO$_2$_TS_6Å	-246.2000	0.8000	-245.4100
Cu_NH$_2$+CO$_2$_TS_7Å	-245.8310	0.8086	-245.0200
Cu_NH$_2$+CO$_2$_TS_8Å	-245.6100	0.8100	-244.8000
Cu_NH$_2$+CO$_2$_TS_bare	-142.1317	0.7695	-141.3622
Cu_NH$_2$+COOH_TS_5Å	-250.0100	1.0900	-248.9300
Cu_NH$_2$+COOH_TS_6Å	-249.3100	1.0900	-248.2200
Cu_NH$_2$+COOH_TS_7Å	-248.8600	1.1300	-247.7300
Cu_NH$_2$+COOH_TS_8Å	-248.6600	1.1300	-247.5200
Cu_NH$_2$+COOH_TS_bare	-145.2206	1.1301	-144.0905
Cu_NH$_2$+CO_TS_5Å	-239.0300	0.6600	-238.3700
Cu_NH$_2$+CO_TS_6Å	-238.6100	0.6800	-237.9300
Cu_NH$_2$+CO_TS_7Å	-238.3000	0.6900	-237.6100
Cu_NH$_2$+CO_TS_8Å	-238.1100	0.6900	-237.4200
Cu_NH$_2$+CO_TS_bare	-134.6736	0.6849	-133.9887
Cu_NO+CO$_2$_product_5Å	-246.0000	0.4274	-245.2500
Cu_NO+CO$_2$_product_6Å	-244.6100	0.3800	-244.2300
Cu_NO+CO$_2$_product_7Å	-243.9000	0.3800	-243.5200
Cu_NO+CO$_2$_product_8Å	-243.6000	0.3700	-243.2400
Cu_NO+CO$_2$_product_bare	-139.9545	0.3540	-139.6004
Cu_NO+COOH_product_5Å	-249.0000	0.6420	-248.2600
Cu_NO+COOH_product_6Å	-248.5700	0.6900	-247.8800
Cu_NO+COOH_product_7Å	-248.3200	0.7100	-247.6100
Cu_NO+COOH_product_8Å	-248.0900	0.7200	-247.3700
Cu_NO+COOH_product_bare	-144.5613	0.7146	-143.8467
Cu_NO+CO_product_5Å	-238.0000	0.2588	-237.6900
Cu_NO+CO_product_6Å	-236.4000	0.2000	-236.2000
Cu_NO+CO_product_7Å	-235.9500	0.2100	-235.7400
Cu_NO+CO_product_8Å	-235.9500	0.1900	-235.7600

Cu_NO+CO_product_bare	-132.2386	0.2060	-132.0326
Cu_NOH+CO$_2$_product_5Å	-250.0000	0.7142	-248.8700
Cu_NOH+CO$_2$_product_6Å	-248.7800	0.6500	-248.1300
Cu_NOH+CO$_2$_product_7Å	-248.1300	0.6700	-247.4600
Cu_NOH+CO$_2$_product_8Å	-247.8900	0.6800	-247.2100
Cu_NOH+CO$_2$_product_bare	-144.3481	0.6713	-143.6769
Cu_NOH+COOH_product_5Å	-252.0000	0.9482	-250.8800
Cu_NOH+COOH_product_6Å	-252.2400	0.9600	-251.2800
Cu_NOH+COOH_product_7Å	-252.0900	0.9900	-251.1000
Cu_NOH+COOH_product_8Å	-251.8600	1.0000	-250.8600
Cu_NOH+COOH_product_bare	-148.2915	0.9904	-147.3011
Cu_NOH+CO_product_5Å	-241.0000	0.5173	-240.5300
Cu_NOH+CO_product_6Å	-240.6900	0.5200	-240.1800
Cu_NOH+CO_product_7Å	-240.3000	0.5500	-239.7600
Cu_NOH+CO_product_8Å	-240.0800	0.5500	-239.5300
Cu_NOH+CO_product_bare	-136.7453	0.5592	-136.1861
Cu_N+CO$_2$_product_5Å	-240.0000	0.3600	-239.9700
Cu_N+CO$_2$_product_6Å	-238.6100	0.2900	-238.3100
Cu_N+CO$_2$_product_7Å	-237.9700	0.3100	-237.6600
Cu_N+CO$_2$_product_8Å	-237.6800	0.3100	-237.3700
Cu_N+CO$_2$_product_bare	-134.0787	0.2836	-133.7951
Cu_N+COOH_product_5Å	-243.0000	0.5954	-242.3900
Cu_N+COOH_product_6Å	-242.6700	0.6300	-242.0400
Cu_N+COOH_product_7Å	-242.4400	0.6400	-241.8000
Cu_N+COOH_product_8Å	-242.2100	0.6500	-241.5600
Cu_N+COOH_product_bare	-138.6436	0.6428	-138.0009
Cu_N+CO_product_5Å	-232.0000	0.1848	-232.0200
Cu_N+CO_product_6Å	-231.9600	0.2000	-231.7600

Cu_N+CO_product_7Å	-231.7200	0.2100	-231.5100
Cu_N+CO_product_8Å	-231.5100	0.2000	-231.3100
Cu_N+CO_product_bare	-128.0121	0.2016	-127.8105
Cu_NH+CO$_2$_product_5Å	-244.0000	0.6477	-243.4800
Cu_NH+CO$_2$_product_6Å	-243.3100	0.6200	-242.6900
Cu_NH+CO$_2$_product_7Å	-242.7700	0.6600	-242.1100
Cu_NH+CO$_2$_product_8Å	-242.5300	0.6600	-241.8800
Cu_NH+CO2_product_bare	-139.0001	0.6413	-138.3589
Cu_NH+COOH_product_5Å	-247.0000	0.8898	-246.2200
Cu_NH+COOH_product_6Å	-247.0500	0.9300	-246.1100
Cu_NH+COOH_product_7Å	-246.9200	0.9500	-245.9700
Cu_NH+COOH_product_8Å	-246.6700	0.9500	-245.7100
Cu_NH+COOH_product_bare	-142.9512	0.9191	-142.0322
Cu_NH+CO_product_5Å	-236.0000	0.5182	-235.8700
Cu_NH+CO_product_6Å	-235.1700	0.4500	-234.7200
Cu_NH+CO_product_7Å	-234.8000	0.4600	-234.3400
Cu_NH+CO_product_8Å	-234.6200	0.4600	-234.1600
Cu_NH+CO_product_bare	-131.1861	0.4588	-130.7273
Cu_NH$_2$+CO$_2$_product_5Å	-248.0000	0.9266	-246.8500
Cu_NH$_2$+CO$_2$_product_6Å	-247.1200	0.9200	-246.2000
Cu_NH$_2$+CO$_2$_product_7Å	-246.5800	0.9200	-245.6600
Cu_NH$_2$+CO$_2$_product_8Å	-246.3500	0.9200	-245.4300
Cu_NH$_2$+CO$_2$_product_bare	-142.8075	0.9154	-141.8922
Cu_NH$_2$+COOH_product_5Å	-251.0000	1.1717	-249.8800
Cu_NH$_2$+COOH_product_6Å	-250.6500	1.1400	-249.5100
Cu_NH$_2$+COOH_product_7Å	-250.4100	1.1600	-249.2500
Cu_NH$_2$+COOH_product_8Å	-250.1000	1.1600	-248.9400
Cu_NH$_2$+COOH_product_bare	-146.5496	1.1749	-145.3747

Cu_NH$_2$+CO_product_5Å	-240.0000	0.7347	-238.8800
Cu_NH$_2$+CO_product_6Å	-239.3900	0.7700	-238.6200
Cu_NH$_2$+CO_product_7Å	-239.0800	0.7900	-238.2900
Cu_NH$_2$+CO_product_8Å	-238.8400	0.7900	-238.0500
Cu_NH$_2$+CO_product_bare	-135.3388	0.7710	-134.5678
Cu_H_6Å	-210.7600	0.1700	-210.5900
Cu_H_7Å	-210.5300	0.1700	-210.3600
Cu_H_8Å	-210.4100	0.1700	-210.2400

Table S6. Free energies for each isolated molecule calculated using VASP for electronic energy and Gaussian16 for thermo-correction

Species	E_{elect}	Thermo	G (eV)
CO$_2$	-23.0097	-0.0094	-23.2654
H$_2$	-6.7616	-0.0016	-6.8041

References

1   Y. Huang, R. Yang, C. Wang, N. Meng, Y. Shi, Y. Yu and B. Zhang, *ACS Energy Lett.*, 2022, **7**, 284-291.
2   M. Shibata and N. Furuya, *J. Electroanal. Chem.*, 2001, **507**, 177-184.
3   D. Saravanakumar, J. Song, S. Lee, N. H. Hur and W. Shin, *ChemSusChem*, 2017, **10**, 3999-4003.
4   C. Lv, L. Zhong, H. Liu, Z. Fang, C. Yan, M. Chen, Y. Kong, C. Lee, D. Liu, S. Li, J. Liu, L. Song, G. Chen, Q. Yan and G. Yu, *Nat. Sustain.*, 2021, **4**, 868-876.
5   H. Wang, Y. Jiang, S. Li, F. Gou, X. Liu, Y. Jiang, W. Luo, W. Shen, R. He and M. Li, *Appl. Catal. B*, 2022, **318**, 121819.
6   J. Leverett, T. Tran-Phu, J. A. Yuwono, P. Kumar, C. Kim, Q. Zhai, C. Han, J. Qu, J. Cairney, A. N. Simonov, R. K. Hocking, L. Dai, R. Daiyan and R. Amal, *Adv. Energy Mater.*, 2022, **12**, 2201500.
7   X. Zhang, X. Zhu, S. Bo, C. Chen, M. Qiu, X. Wei, N. He, C. Xie, W. Chen, J. Zheng, P. Chen, S. P. Jiang, Y. Li, Q. Liu and S. Wang, *Nat. Commun.*, 2022, **13**, 5337.
8   S. Zhang, J. Geng, Z. Zhao, M. Jin, W. Li, Y. Ye, K. Li, G. Wang, Y. Zhang, H. Yin, H. Zhang and H. Zhao, *EES Catal.*, 2023, DOI: 10.1039/D2EY00038E.
9   N. Cao, Y. Quan, A. Guan, C. Yang, Y. Ji, L. Zhang and G. Zheng, *J. Colloid Interface Sci.*, 2020, **577**, 109-114.
10 Y. Feng, H. Yang, Y. Zhang, X. Huang, L. Li, T. Cheng and Q. Shao, *Nano Lett.*, 2020, **20**, 8282-8289.
11 N. Meng, Y. Huang, Y. Liu, Y. Yu and B. Zhang, *Cell Rep. Phys. Sci.*, 2021, **2**, 100378.
12 D. B. Kayan and F. Köleli, *Appl. Catal. B*, 2016, **181**, 88-93.
13 C. Chen, X. Zhu, X. Wen, Y. Zhou, L. Zhou, H. Li, L. Tao, Q. Li, S. Du, T. Liu, D. Yan, C. Xie, Y. Zou, Y. Wang, R. Chen, J. Huo, Y. Li, J. Cheng, H. Su, X. Zhao, W. Cheng, Q. Liu, H. Lin, J. Luo, J. Chen, M. Dong, K. Cheng, C. Li and S. Wang, *Nat. Chem.*, 2020, **12**, 717-724.
14 M. Yuan, J. Chen, Y. Bai, Z. Liu, J. Zhang, T. Zhao, Q. Wang, S. Li, H. He and G. Zhang, *Angew. Chem., Int. Ed.*, 2021, **60**, 10910-10918.
15 M. Yuan, J. Chen, Y. Bai, Z. Liu, J. Zhang, T. Zhao, Q. Shi, S. Li, X. Wang and G. Zhang, *Chem. Sci.*, 2021, **12**, 6048-6058.
16 M. Yuan, J. Chen, Y. Xu, R. Liu, T. Zhao, J. Zhang, Z. Ren, Z. Liu, C. Streb, H. He, C. Yang, S. Zhang and G. Zhang, *Energy Environ. Sci.*, 2021, **14**, 6605-6615.
17 M. Yuan, H. Zhang, Y. Xu, R. Liu, R. Wang, T. Zhao, J. Zhang, Z. Liu, H. He, C. Yang, S. Zhang and G. Zhang, *Chem. Catal.*, 2022, **2**, 309-320.